



**Experimental and Simulation Study  
Results for Video Landmark Acquisition  
and Tracking Technology**

**Roger T. Schappell, John C. Tietz,  
H. Michael Thomas, and James W. Lowrie**

MARTIN MARIETTA CORPORATION  
Denver, Colorado 80201

Contract No. NAS1-14489  
February 1979



National Aeronautics and  
Space Administration

**Langley Research Center**  
Hampton, Virginia 23665  
AC 804 827-3966

LIBRARY COPY

LANGLEY RESEARCH CENTER  
LIBRARY  
HAMPTON, VIRGINIA



## FOREWORD

---

This report presents the experimental and simulation study results for Video Landmark Acquisition and Tracking Technology applicable to future global monitoring systems. During this study, a number of related technology areas were investigated and are summarized herein. Earlier work performed during the first six months of the contract was reported in *Preliminary Experiment Definition for Video Landmark Acquisition and Tracking*, NAS CR-145122, December 1976, by Schappell, Tietz, and Hulstrom.

CONTENTS

---

	<u>Page</u>
I. INTRODUCTION . . . . .	1
II. FEATURE IDENTIFICATION AND LOCATION EXPERIMENT (FILE). .	3
A. Principle of Operation . . . . .	3
B. Experiment Description . . . . .	5
C. Hardware Description . . . . .	6
D. Expected Results . . . . .	8
III. FILE TRADEOFF STUDIES . . . . .	9
A. Tape Recorder Selection . . . . .	9
B. Film Camera Selection . . . . .	9
C. TV Camera Selection . . . . .	9
D. Terminator and Sunrise Sensing Tradeoff . . . . .	14
IV. FILE PERFORMANCE ANALYSIS . . . . .	16
A. Decision Threshold Selection . . . . .	16
B. Field Measurements versus Analytical Model Results . . .	23
C. Error-Rate Analysis . . . . .	25
D. Data-Taking Interval Analysis . . . . .	26
V. ADVANCED FILE CONCEPT . . . . .	30
A. Coastline Tracking Algorithm . . . . .	30
B. Recommended Implementation for Surface-Feature Tracking . . . . .	43
VI. NEW CONCEPTS FOR ADVANCED FILE-TYPE EXPERIMENTS . . . .	57
A. Landmark Registration Simulation . . . . .	57
B. Advanced FILE Simulation (Multicolor Registration) . . .	68
VII. CONCLUSIONS AND RECOMMENDATIONS . . . . .	75
VIII. REFERENCES . . . . .	77

Figure

---

1	Target Spectral Radiances . . . . .	4
2	99% Confidence Polygons, Sun 41 to 60° from Zenith . . .	5
3	FILE System General Arrangement . . . . .	6
4	FILE System Block Diagram . . . . .	7
5	TV Camera Constraints . . . . .	12
6	Cumulative Probability Ogives for Fairchild CCD202 for 5-km Visibility, 0 to 60° Orbit Angle . . . . .	17
7	Cumulative Probability Ogives for Fairchild CCD202 for 23-km Visibility, 0 to 60° Orbit Angle . . . . .	17

8	Cumulative Probability Ogives for Fairchild CCD202 for 5-km Visibility, 41 to 60° Orbit Angle, 650 nm . . . . .	18
9	Cumulative Probability Ogives for Fairchild CCD202 for 23-km Visibility, 41 to 60° Orbit Angle, 650 nm . . . . .	18
10	Cumulative Probability Ogives for Fairchild CCD202 for 5-km Visibility, 0 to 41° Orbit Angle, 650 nm . . . . .	19
11	Cumulative Probability Ogives for Fairchild CCD202 for 23-km Visibility, 0 to 41° Orbit Angle, 650 nm . . . . .	19
12	Cumulative Probability Ogives for Fairchild CCD202 for 5-km Visibility, 41 to 60° Orbit Angle, 850 nm . . . . .	20
13	Cumulative Probability Ogives for Fairchild CCD202 for 23-km Visibility, 41 to 60° Orbit Angle, 850 nm . . . . .	20
14	Cumulative Probability Ogives for Fairchild CCD202 for 5-km Visibility, 0 to 41° Orbit Angle, 850 nm . . . . .	21
15	Cumulative Probability Ogives for Fairchild CCD202 for 23-km Visibility, 0 to 41° Orbit Angle, 850 nm . . . . .	21
16	99% Confidence Polygons, Sun 0 to 41° from Zenith . . . . .	23
17	World Map (without clouds) . . . . .	27
18	Small Cloud Model (typical run) . . . . .	28
19	Medium Cloud Model (typical run) . . . . .	28
20	Large Cloud Model (typical run) . . . . .	28
21	Scan Configuration . . . . .	30
22	Circuitry for Computing Vector Components . . . . .	32
23	Vector Length as a Function of Wavelength for Various Interfaces . . . . .	35
24	Blue/Infrared Vector Pairs for Various Interfaces . . . . .	35
25	Multispectral Scanning Scheme . . . . .	36
26	Record of Track Produced by Algorithm . . . . .	37
27	LANDSAT Image of Chesapeake Bay . . . . .	37
28	Tracking Angle versus Photocathode Emission . . . . .	40
29	Error Angle versus Contrast for Various Current Densities . . . . .	40
30	99.5% Confidence Limits for Observed Vector Length versus True Vector Length at Various Current Densities . . . . .	41
31	Vector Standard Deviation versus Photocathode Current Density for Two Scan Rates . . . . .	42
32	VILAT Processor Block Diagram . . . . .	46
33	VILAT Processor 4K Memory Module Logic Diagram . . . . .	47
34	VILAT Processor Central Control Unit Logic Diagram . . . . .	48
35	VILAT Processor Microprogrammer Memory Logic Diagram . . . . .	49
36	VILAT Processor Arithmetic and Logic Unit Logic Diagram . . . . .	50

37	VILAT Processor Memory Address Register	
	Logic Diagram . . . . .	51
38	VILAT Processor Clock Control and PROM Memory . . . . .	
	Logic Diagram . . . . .	52
39	VILAT Processor I/O Data Bus and Keyboard	
	Logic Diagram . . . . .	53
40	VILAT Processor Breadboard Interface Logic Diagram . . .	54
41	Image Processing Facility . . . . .	58
42	Relationship between Landmark and Search Area . . . . .	59
43	Registration of Area Landmark . . . . .	60
44	Organization of Landmark Identification Program . . . . .	62
45	Correlation Algorithms . . . . .	63
46	Two-Dimensional Resampling of Intensity Curve . . . . .	64
47	Resampling Algorithms . . . . .	65
48	Effects of Cloud Coverage . . . . .	68
49	Selection of Search Area . . . . .	70
50	Display of Search Area . . . . .	71
51	Selection of Landmark Area . . . . .	72
52	Display of Landmark Area . . . . .	73
53	Display Correlation Results . . . . .	74

Table

---

1	Preliminary FILE Program Candidate Tape Recorders . . .	10
2	Candidate TV Cameras and Sensors . . . . .	11
3	Comparison of Field Measurements with FILE	
	Design Model (summer) . . . . .	24
4	Classification Errors . . . . .	25
5	VILAT Processor Instruction Set . . . . .	45
6	Whole-Pixel Search Timing Requirements . . . . .	66
7	Subpixel Resample and Search Timing Requirements . . . . .	66
8	Sample Outline of VILAT Development Plan . . . . .	76

# I. INTRODUCTION

---

Studies relating to Earth and stellar exploration programs have pointed out the need for adaptive real-time observation systems capable of detection, acquisition, pointing, and tracking with respect to the observable of interest, with emphasis on autonomous operation.

This report provides a synopsis of related Earth observation technology that was developed, breadboarded, and tested under contract to NASA and includes surface-feature tracking, generic feature classification and landmark identification, and navigation by multicolor correlation.

With the advent of the Space Shuttle era, the NASA role takes on new significance in that one can now conceive of dedicated Earth resources missions. Space Shuttle will also provide a unique test bed for evaluating advanced sensor technology like that described in this report. As a result of this type of rationale, the FILE OSTA-1 Shuttle experiment, which grew out of the Video Landmark Acquisition and Tracking (VILAT) activity, was developed and is described in this report along with the relevant tradeoffs. In addition, a synopsis of FILE computer simulation activity is included. This synopsis relates to future required capabilities such as landmark registration, reacquisition, and tracking.

Many tasks have been performed under this contract. Though they all relate to landmark identification and tracking, they are not closely related and are therefore presented in five separate chapters.

Chapter II deals with the Feature Identification and Location Experiment (FILE), which was defined under this contract. FILE hardware is being built, with the intent of flying it on STS-2 or -3.

Chapter III summarizes the results of a number of largely independent tradeoff studies performed in the definition of the FILE. These tradeoffs were required to select certain major system components.

Chapter IV reports the results of a number of FILE system performance analyses, including target signature analyses; determination of the effects of camera noise, viewing angles, atmospheric effects, position in orbit, and "beta" angles; estimation of system error rate; and an analysis of data acquired as a function of time.

Chapter V describes a unique approach to video landmark acquisition and tracking, and contains a summary of analyses and experiments conducted to estimate the performance of a system based on this approach. It also describes a hardware system to locate and track landmarks by means of the principles described. Such an instrument is recommended as an advanced Feature Identification and Location Experiment to be flown aboard the Space Shuttle. Chapter VI reports the results of experiments performed by Martin Marietta's image processing facility to test concepts for eventual incorporation in an advanced FILE instrument.

## II. FEATURE IDENTIFICATION AND LOCATION EXPERIMENT (FILE)

The FILE goal is to test a technique for classifying picture elements in a television picture of the Earth as vegetation, bare land, water, or clouds and snow. Classification will be automatic and in real time by a small instrument. The technique uses simple circuitry that is adaptable to a variety of applications and requires no computational capability. The experiment also tests the ability of the instrument to make appropriate real-time acquisition decisions based on scene contents.

### A. PRINCIPLE OF OPERATION

The FILE system classifies on a picture-element-by-picture-element basis. Each element is classified by its spectral signature alone. No pattern recognition is required. Computer simulations and field measurements have confirmed that the four basic feature types--vegetation, bare land, water, and clouds or snow--can be separated by radiance measurements at two discrete wavelengths: 650 and 850 nanometers. The former wavelength is in the chlorophyll absorption band, in which healthy green vegetation has very low reflectance. At this wavelength, water has significant reflectance; and bare land, snow and clouds have even higher reflectance. Eight hundred fifty nanometers is in the near infrared, where healthy green vegetation has a very high reflectance, as do clouds, snow, and bare land, while water has extremely low reflectance, as illustrated in Figure 1.

Observed radiance from an object is a function of the object's reflectance and incident illumination, as well as radiance and absorption of the column of air through which the object is viewed. However, the *ratio* of the radiances at the two wavelengths is reasonably independent of factors other than reflectance. Water and vegetation can be separated from clouds, snow, and bare land on the basis of this ratio alone. However, the radiance ratio for bare land is essentially the same as that for clouds and snow so these features must be separated on the basis of absolute radiance. This can be done with only a rough estimate of the solar illumination angle. The reflectances of clouds and snow are much higher than most bare-land reflectances. Errors will be made in the case of such highly reflective features as limestone and white sand, but such features constitute a small fraction of the Earth's surface.

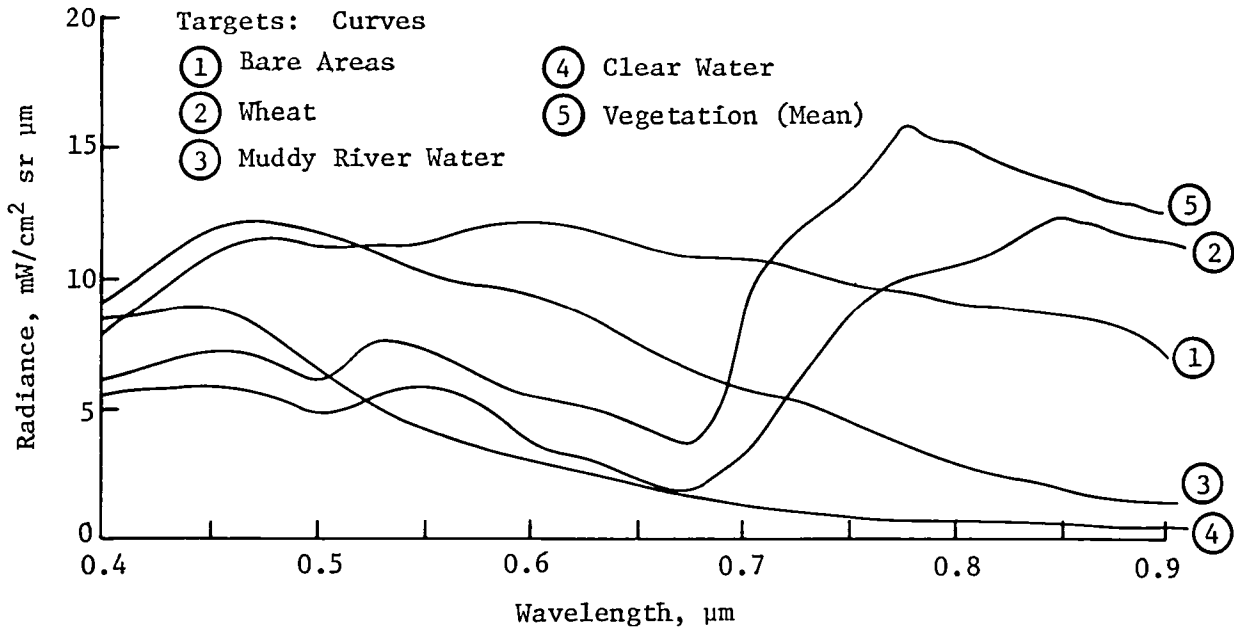


Figure 1 Target Spectral Radiances

Figure 2 illustrates how readily the various types of features can be separated. The figure was based on a computer model that considered such factors as visibility (as low as 5 km) illumination angle (from  $0^\circ$  or normal to the Earth's surface to  $41^\circ$ ), sensor noise, pixel nonuniformity and dark current, viewing angles up to  $5^\circ$  from normal, a variety of vegetation and bare land types, and 2 degrees of water turbidity. Although the polygons in Figure 2 overlap to a certain extent, because they represent 99% confidence limits the majority of cases can be expected to fall in unambiguous points on the plane. The analysis indicates that a classification accuracy of better than 95% can be expected for pure signatures under typical viewing conditions. As previously mentioned, certain types of features such as limestone will be misclassified and certain mixed features such as winter forests, extremely distressed vegetation, and swampland have no unique classification. However, the accuracy achieved is expected to be adequate for a wide variety of applications.

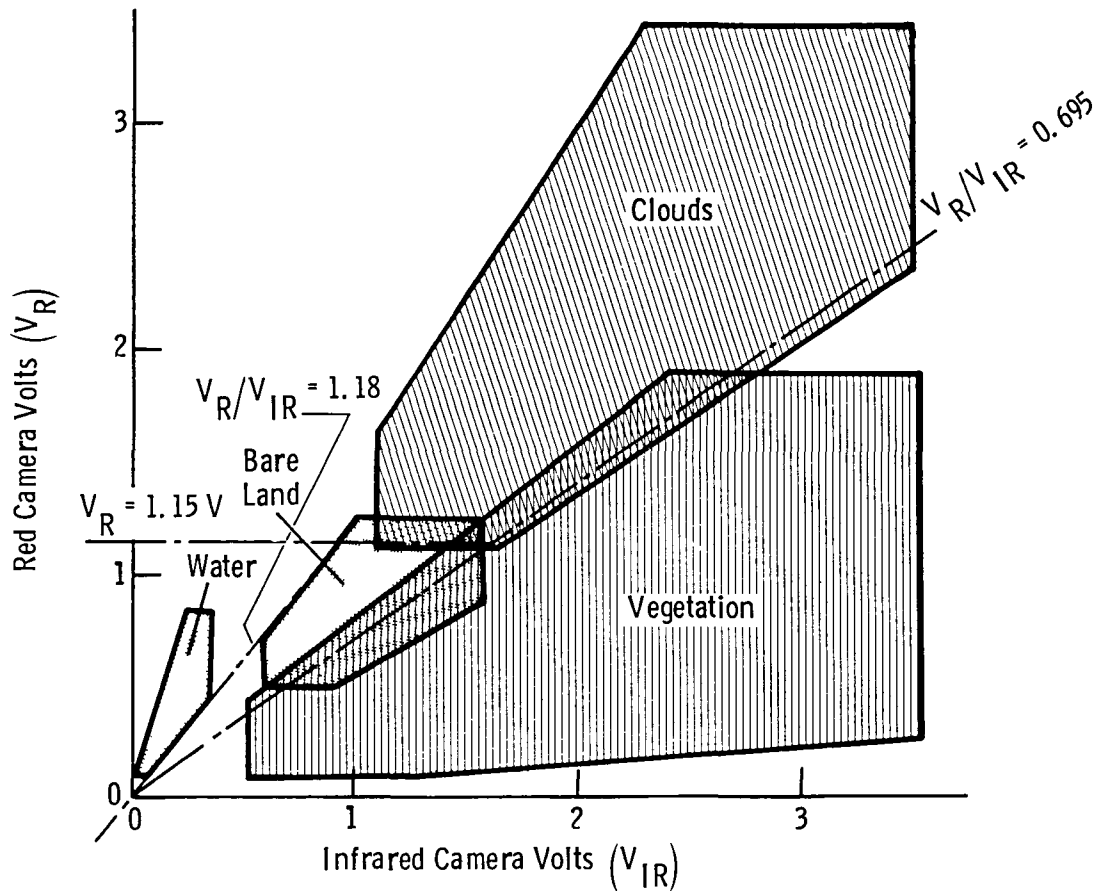


Figure 2 99% Confidence Polygons, Sun 41 to 60° from Zenith

B. EXPERIMENT DESCRIPTION

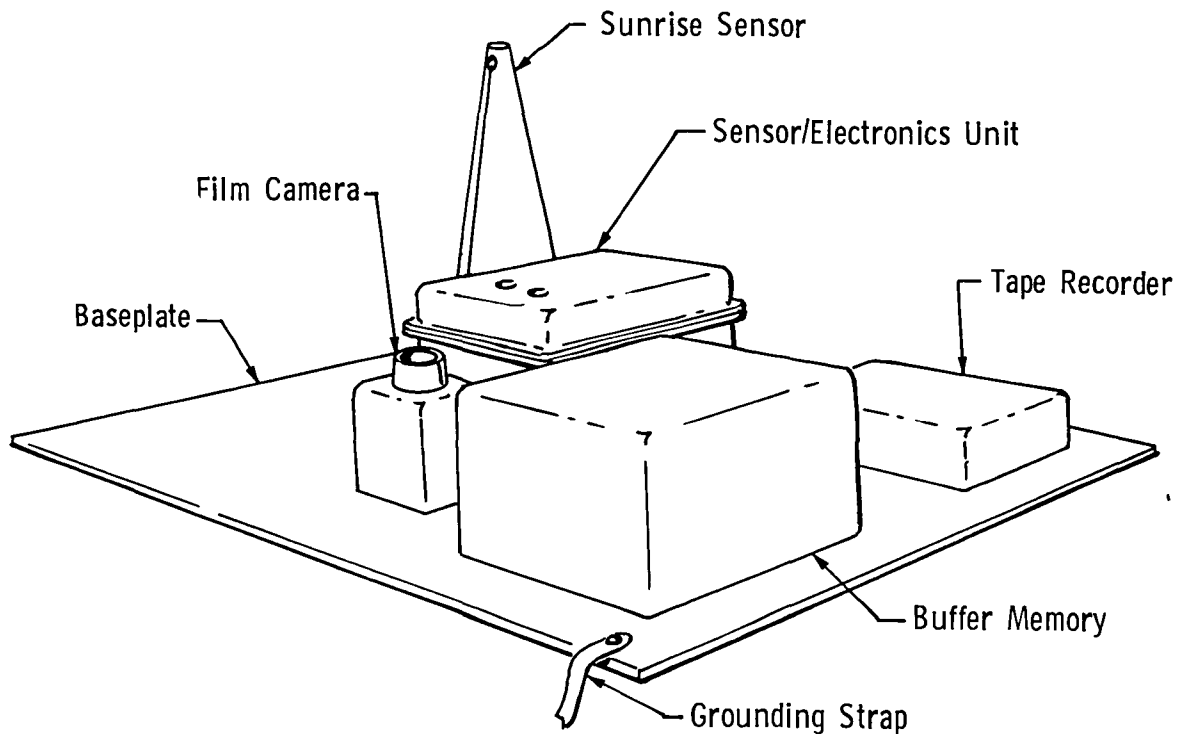
The FILE experiment will test the previously described classification technique by observing the Earth from orbit aboard the Space Shuttle, using two boresighted CCD television cameras. The cameras will view through optical filters for 650 and 850 nanometers, respectively. Approximately 120 frames of data will be stored on tape in a recorder that is an integral part of the experiment. Data for each frame will include digitized television images from the two cameras, a count of the number of picture elements in the scene that were classified in each category, and the date and time of day (from which the scene's latitude and longitude can be determined). For comparison, a 70-mm film camera will take a color picture for each data frame.

To test the ability of the system to make real-time data acquisition decisions, and to increase the variety of the data returned, the instrument will count the number of frames of data representing scenes that are predominantly either water and clouds or bare land. It will not record data for scenes in either of these classes after 32 frames have been taken.

From the data, a four-color hard-copy picture can be constructed for each data frame for comparison with the corresponding photograph. The data will be analyzed to determine classification accuracy, reasons for misclassifications, and appropriate adjustments to decision thresholds.

### C. HARDWARE DESCRIPTION

The FILE system comprises five hardware assemblies, which are fastened to a single baseplate to facilitate handling (Fig. 3).



**Note: Multilayer insulation/beta cloth cover not shown.**

*Figure 3 FILE System General Arrangement*

The sensor and electronics unit contains television cameras and decision-making electronics, controls the entire experiment, and is the only interface with the Shuttle. Figure 4 is a block diagram of the unit. It receives power and a GMT time signal from the Shuttle and sunlight through a light pipe from the sunrise sensor mast to inhibit operation on the dark side of the Earth. It sends data to the tape recorder via a buffer memory, and produces control signals to operate the film camera and buffer memory.

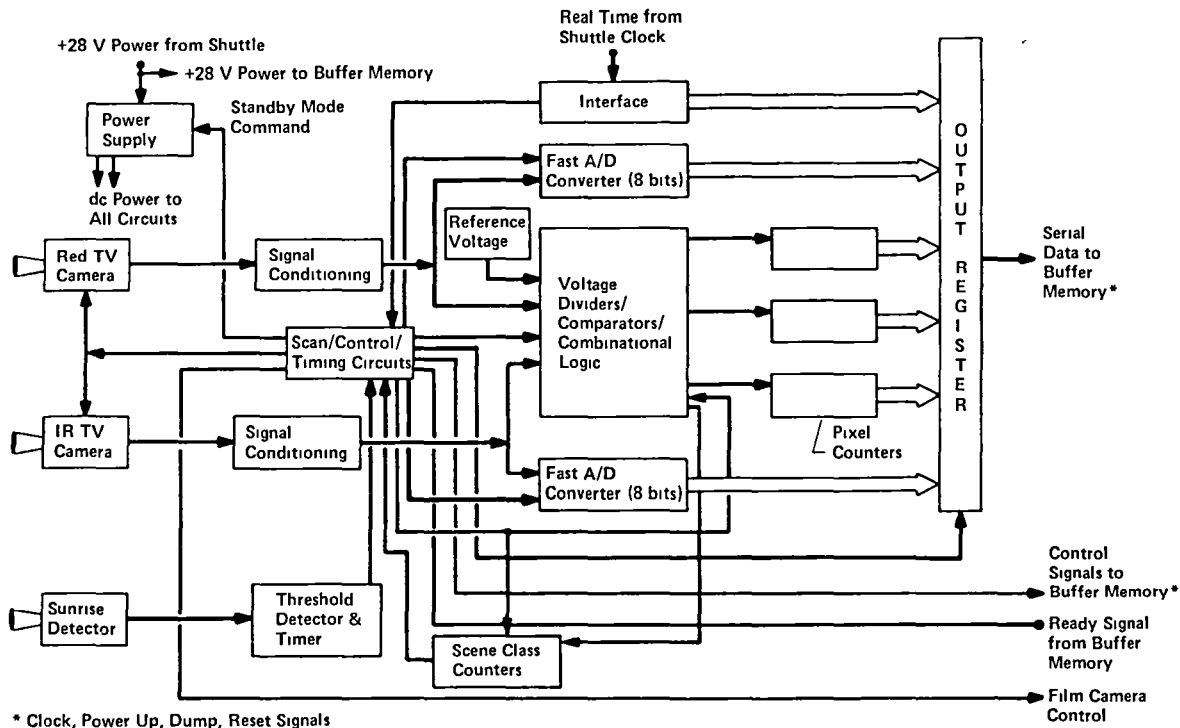


Figure 4 FILE System Block Diagram

The television field of view is  $18^\circ \times 23^\circ$ , which corresponds to an area of  $9300 \text{ km}^2$  on the ground. Each picture element therefore corresponds to an area of approximately  $1 \text{ km}^2$ . The film camera has a  $32^\circ$  square field of view, which corresponds to  $25,000 \text{ km}^2$  on the ground, and a 100-m resolution can be expected.

Classification decisions are made by using voltage dividers on the camera outputs, comparators, and a reference voltage. Comparator outputs are logically combined, producing gating signals to route clock pulses to pixel counters corresponding to the various types of features.

The buffer memory accepts the higher data rate from the sensor and electronics unit and plays it out at a much lower rate that can be accepted by the tape recorder.

D. EXPECTED RESULTS

The FILE experiment is expected to establish the practicality of making autonomous real-time decisions for satellite data acquisition by means of a simple technique for scene analysis. The experiment is intended to be the first in a series of progressively more sophisticated experiments leading to an adaptive real-time search, identification, and pointing system with the objective of providing a significant reduction in the end-to-end data management problem through selective data acquisition.

### III. FILE TRADEOFF STUDIES

---

A number of tradeoff studies were performed under this contract to select components for the FILE experiment. Components include the tape recorder, film camera, and TV cameras.

#### A. TAPE RECORDER SELECTION

Table 1 is a list of tape recorders considered. Some recorders would require extensive modification to survive in the environment and operate from 28 Vdc. Any of the candidate recorders would represent a significant fraction of the total cost of the experiment. Therefore, when it was learned that a Lockheed model 4200 recorder could be acquired from NASA, the decision was obviously in favor of this recorder. It has the storage capacity required, was designed for the environment, and will be available when required for the experiment.

#### B. FILM CAMERA SELECTION

The film camera decision was also based on the availability of a suitable space-qualified camera at no cost. Two such cameras were available--a 70-mm Hasselblad camera and a 16-mm camera. The latter would give poorer resolution, and the manufacturer is no longer in business, so replacement parts procurement was a potential problem. The Hasselblad camera was therefore selected.

#### C. TV CAMERA SELECTION

Many TV cameras are available at moderate cost. Table 2 shows the characteristics of eight representative cameras that were considered. The field was considerably narrowed by FILE system requirements for linear (unity gamma) response and sensitivity from 650 to 850 nanometers, the desirability of low-voltage operation, low-noise, 40:1 dynamic range, and cost--all of which pointed to solid-state arrays.

Table 1 Preliminary FILE Program Candidate Tape Recorders

Recorder	Frequency and Type	Available Recording Time	Design Environment	Weight, lb	Availability	Cost, \$
Lockheed Type 4200 (modified)	500-kHz analog, 4 tracks	600 to 1100 frames	Space Shuttle	7	6 months (with modifications)	24k recorder 4k ground playback
Ampex AR 728 (modified for Skylab)	1-mbps digital, 28 tracks	24 minutes	Aircraft (modified for space)	90 as modified	Skylab spares only (not located)	Possible GFE (if located)
Sony Beta Max SL 6200	4.50MHz analog	60 minutes	Ground	45.2	Commercial off-shelf	1300 list (plus mods)
AKAI VTS-100S	4.5-MHz analog	23.5 minutes	Ground	11	Commercial off-shelf	1100 list (plus mods)
RCA Star 3	5.0-MHz analog	60 minutes	Aircraft	40	6 to 7 months	50k
Odetics DDS-3000 (for SCATHA)	8-kbps digital, 2 tracks	720 minutes	Space	14.5	12 to 15 months	90k
Echo Scientific 34 (for SCATHA)	64-kbps digital, 8 tracks	11 minutes	Space	16.5	TBD	TBD

Table 2 Candidate TV Cameras and Sensors

	Manufacturer							
Camera Identification	RCA TC 1150	RCA TC 1155	RCA TC 1160 AD or BD	Fairchild MV-201	General Electric TN-2000	General Electric TN-2200	General Electric TN-3000	Fairchild (chip)
Sensor Identification	SID 51232	SID 51232	SID 52501	CCD 211	CID	CID	CID	CCD 202
Pixels Actual	256 x 320	256 x 320	256 x 320	244 x 190 = 46,360	250 x 200	128 x 128	250 x 200	100 x 100 = 10,000
Pixels Effective	512 x 320 = 163,840	512 x 320 = 163,840	512 x 320 = 163,840	(Later coming) (488 x 380 = 185,440)	500 x 200 = 100,000	128 x 128 = 16,384	500 x 380 = 190,000	100 x 100 = 10,000
Temperature	-12 to 50°C	-12 to 50°C	-12 to 50°C	-50 to 40°C	0 to 50°C	0 to 50°C		-25 to 55°C
Humidity	0 to 90%	0 to 90%	0 to 90%		0 to 90%			--
Weight	2.5 lb plus lens	2.5 lb plus lens	2.2 lb plus lens	12 oz plus lens	43 oz plus lens	18 oz plus lens		--
Size, in	2.75 x 5.88 x 4.5 plus lens	2.75 x 5.88 x 4.5 plus lens	2.75 x 5.88 x 4.5 plus lens	2.5 x 2 x 3.75 plus lens	8.5 x 4.4 x 2.3 plus lens	App 2.4 dia. x 7.3 in., incl lens		24-pin DIP
Power	4 W 12 Vdc	4 W 12 Vdc	4.9 W 12 Vdc	4 W 12 Vdc	9 W to supply 7 W to camera	1.5 W		--
Lens	Built-in, 14 to 45-mm efl	Any C-mount	Any C-mount	Any C-mount	Any C-mount	Any C-mount		Any C-mount
Bias Light	Required (built-in)	Required (built-in)	Required (built-in)	No	No	No	No	No
Cost	Obsolete	Obsolete	AD \$1976 BD \$2950	\$6000	\$2700 to \$3000	Approx \$1000	Less than TN-2000	<\$400
Delivery	30 days	30 days	30 days	Approx 60 days	30 days	Approx 30 days	Early 1978	Approx 30 days

Figure 5 illustrates system constraints that further influenced sensor selection. None of the constraints represents a "hard" limit of practical operation. Rather, the constraints represent reasonable limits in view of system performance goals and implementation decisions that involve many considerations. For example the "smear" limit is based on the rate at which the tape recorder system can accept video information and on A/D conversion speed. These performance limitations were in turn imposed by economic considerations and the desirability of making the tape recorder system convenient to use in future missions. Likewise, the "recognition" limit is a subjective estimate of the number of pixels required for a human observer to adequately recognize the scene during postflight data reduction. In short, the constraints define a reasonable operating area compatible with a number of factors that are peculiar to the experiment.

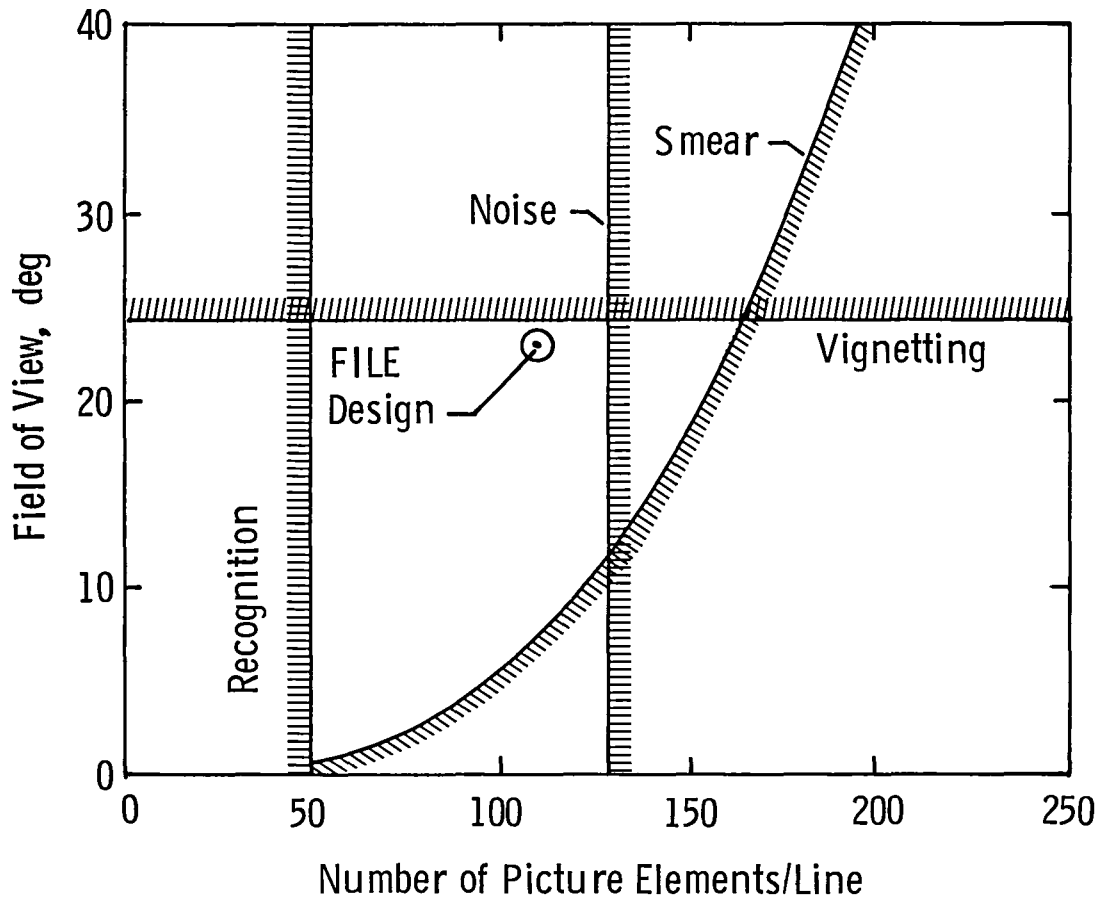


Figure 5 TV Camera Constraints

The upper limit on the number of pixels is partly established by noise considerations. Pixel rate is limited by the recorder and A/D converters, which means that readout time for a complete frame is proportional to the total number of pixels in the frame. For an integrating sensor, this means that dark current starts to become a significant contributor to the signal when the number of pixels becomes excessive; and, while temperature compensation can remove the *average* dark signal from the picture, the dark current *nonuniformity* remains as a source of noise. The limit of 130 pixels per line keeps this nonuniformity noise to a small percentage of normal signal amplitude at expected maximum operating temperature.

This limit is also established by tape-recorder storage capacity. The use of a 100x100 pixel camera instead of, for example, a 320x512 pixel camera allows recording of 16 times more frames. For a tape capacity of 16.1 megabits, this makes the difference between 100 frames and 6 frames. Obviously, many more scenes and viewing conditions can be realized by using a small-format camera. Moreover, a smaller buffer memory can be used with a smaller number of pixels, if such a memory is required because of a limited tape-recorder data rate.

The RCA Big SID camera was eliminated, not only because it has too many pixels, but also because the chip must be floodlighted with a LED light source for proper operation. This so severely limits its dynamic range that it is useless for this application without some form of iris control.

An operating point near the one selected was considered most desirable in terms of postflight data analysis because a wide field of view and many pixels in the scene both facilitate recognition of the observed area.

There are two readily available low-cost sensors that appeared to meet all the requirements, so these were examined in more detail: (1) the GE TN2200 camera, which uses a charge-injection-device (CID) sensor with a 128x128 pixel format; (2) the Fairchild CCD202 chip, a CCD sensor with a 100x100 format. Samples of both were purchased and evaluated. It was found that the Fairchild sensor, with the manufacturer's "evaluation board" support circuitry, produced recognizable images over an illumination range well in excess of 40:1. The image from the CID camera became totally devoid of any detail when light intensity was reduced by a factor of 40 from saturation. This limited range could be compensated for by using a movable iris, but the cost advantage of fixed optics was significant.

Several other factors also favored the CCD chip: (1) support circuitry for scanning and signal processing is less complex; (2) the manufacturer offered good data on the chip; (3) the manufacturer also provided recommended circuits and suggestions. In contrast, the CID is not generally offered without the complete camera, little information about the chip was available (no data sheets), and the manufacturer appeared to be interested only in a mass market for complete systems. Because the existing CID camera design did not appear appropriate for the application, the Fairchild CCD chip was selected.

#### D. TERMINATOR AND SUNRISE SENSING TRADEOFF

It would be desirable to eliminate the FILE sun sensor mast and synchronize FILE system operation with the orbit by sensing the Earth's terminator. This would make the system less dependent on the orbit and Shuttle attitude and would simplify mechanical design problems. The practicality of doing this was examined, but it was determined that it would not be a simple change, for several reasons.

First of all, the sun sensor approach had been studied well before FILE design was begun. Earth-viewing terminator sensors were not considered until it was realized that the FILE was to be mounted in the shade. The former technique could therefore be implemented more quickly. This was a significant consideration in view of the schedule constraints imposed by the planned launch date and available budget.

Second, the spectral-radiance-analysis computer program currently available uses a "flat Earth" model, which is adequate for the FILE camera analysis (with the sun within  $60^\circ$  of zenith and essentially nadir viewing). However, there are no reliable data available to use in setting a threshold for a terminator sensor. Moreover, extrapolation of data from the available model suggested that terminator sensing would not give an accurate indication because clouds near the terminator would tend to turn the instrument on early, whereas water would tend to turn it on late. The error appeared to be on the order of  $\pm 15^\circ$ . The FILE sensor uses absolute radiance to separate clouds from bare land; and, though the radiance "gap" between these types of features is wide, it is desirable to operate the system with the best available data on scene lighting while trying to prove its principles of operation.

Finally, for future flights, FILE can easily be modified to accept an input from a terminator sensor. The only changes would be in the time delay between the sensor signal and the start of operation and in the interface circuitry and connectors to accept the signal. Alternatively, it may be possible to use the camera outputs themselves to make fine adjustments in the cloud/bare-land threshold and thus eliminate the need for coarse Sun angle information.

#### IV. FILE PERFORMANCE ANALYSIS

---

This chapter summarizes the results of the performance analysis for the FILE/OSTA-1 mission.

##### A. DECISION THRESHOLD SELECTION

The FILE system classifies pixels as water, cloud or snow, bare land, or vegetation on the basis of their radiances at two different wavelengths and the ratio of the radiance at one wavelength to the radiance at the other. A computer (T-RAD-1) was used to determine appropriate decision thresholds to use in the flight instrument. As inputs, the program takes target reflectance, reflectance of the area surrounding the target, visibility, angle between a line normal to the Earth's surface and a line to the sun, angle between the line normal to the Earth's surface and the line connecting the observer and target, and the angle between the vertical planes containing the target-sun and target-observer lines. From these data, it determines the path radiance and total radiance observed based on a homogeneous, conservative plane-parallel atmosphere model with a perfectly diffuse surface by application of the double delta function and the Shuster-Schwarzschild approximations. The accuracy of the program has been confirmed by comparison with data taken aboard Skylab.

The T-RAD-1 program was found to be more flexible than necessary. For example, only two wavelengths are of concern, and only one altitude need be modeled. Moreover, it is a large complex program that could not be readily modified to serve as a subroutine in a program that added the effects of sensor pixel nonuniformity, lens systems, dark current, noise, attitude stability and variation of sun angle with orbit position. Therefore, the program was used to establish key data points, and approximating functions were derived by curve fitting for use in an analysis program. The latter program considered the effects of the factors mentioned above and produced cumulative probability ogives (by Monte Carlo analysis) for both radiances and radiance ratio (Fig. 6 through 15). The analysis assumed the orbit to be similar to the baseline OFT-2 orbit as it was known at the time. This orbit has a low "beta" angle, i.e., the line between the Earth and the sun is within a few degrees of the orbit plane.



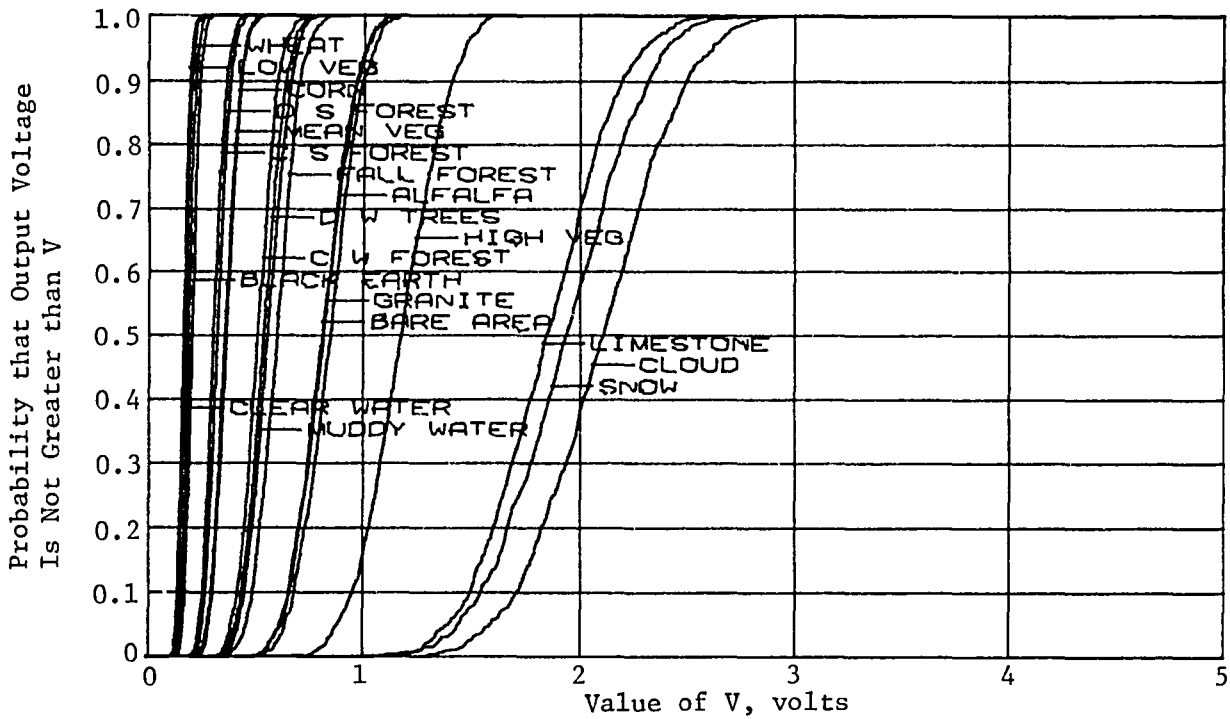


Figure 8 Cumulative Probability Ogives for Fairchild CCD 202 at 5-km Visibility, 41 to 60° Orbit Angle, 650 nm

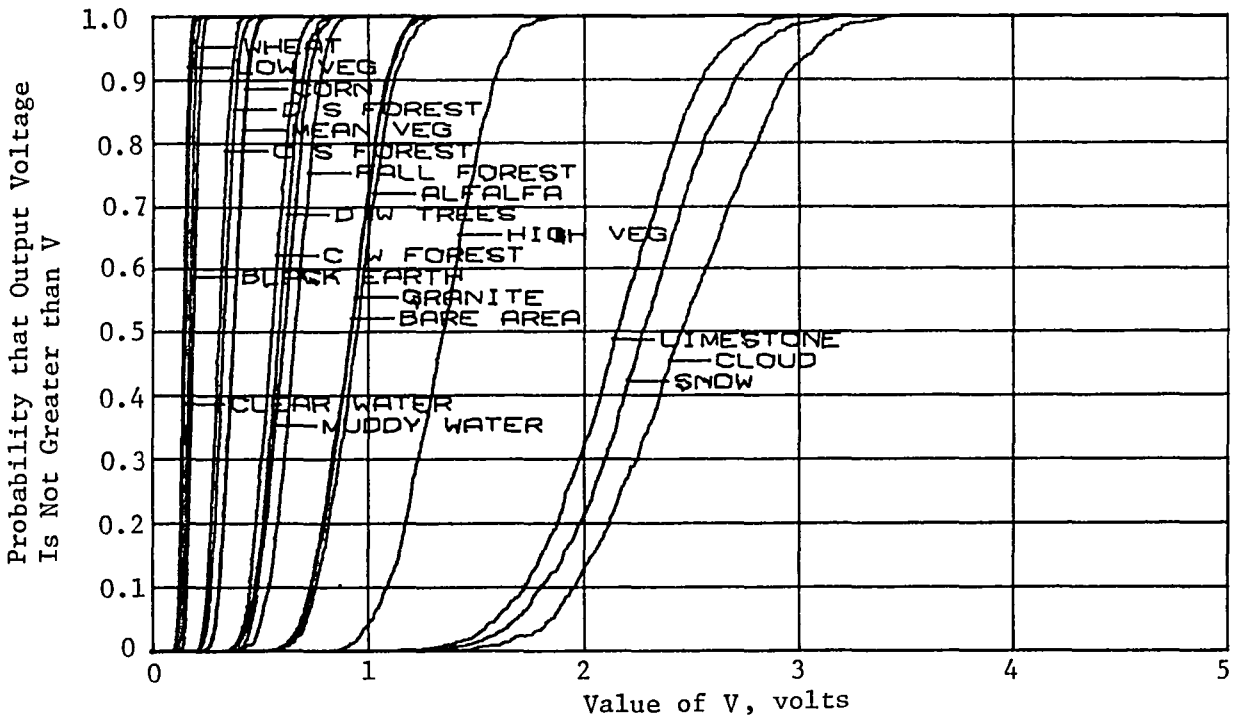


Figure 9 Cumulative Probability Ogives for Fairchild CCD 202 at 23-km Visibility, 41 to 60° Orbit Angle, 650 nm

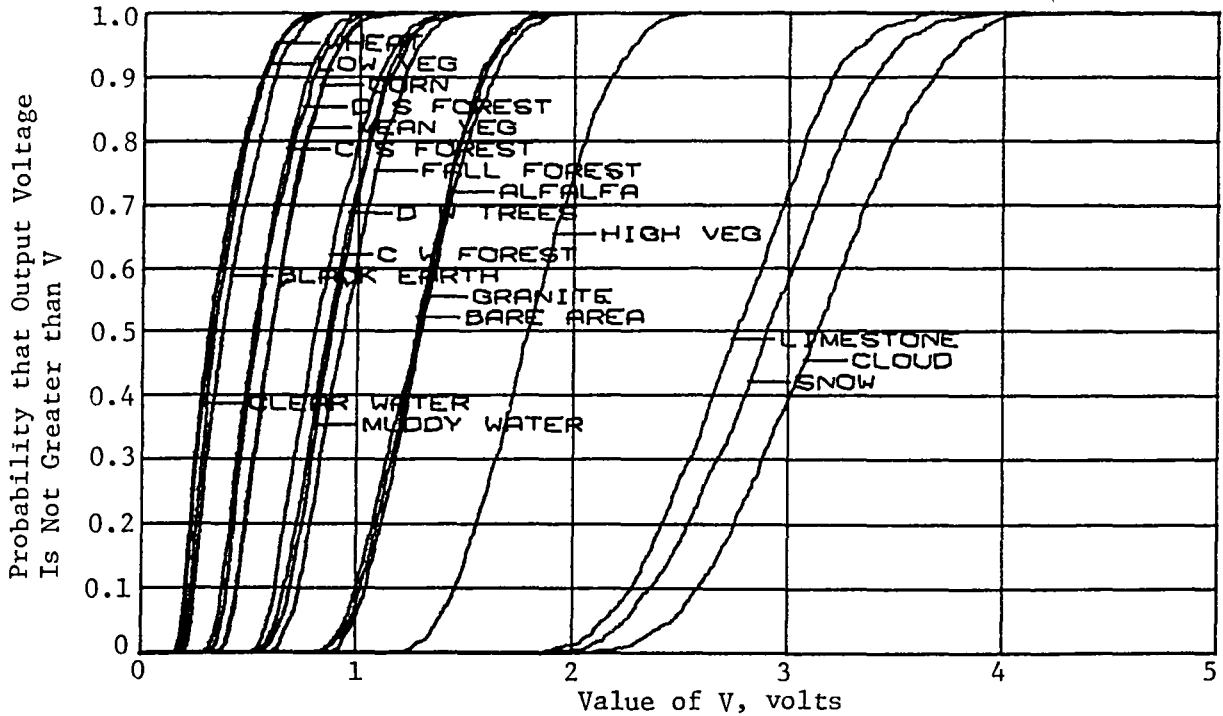


Figure 10 Cumulative Probability Ogives for Fairchild CCD 202 at 5-km Visibility, 0 to 41° Orbit Angle, 650 nm

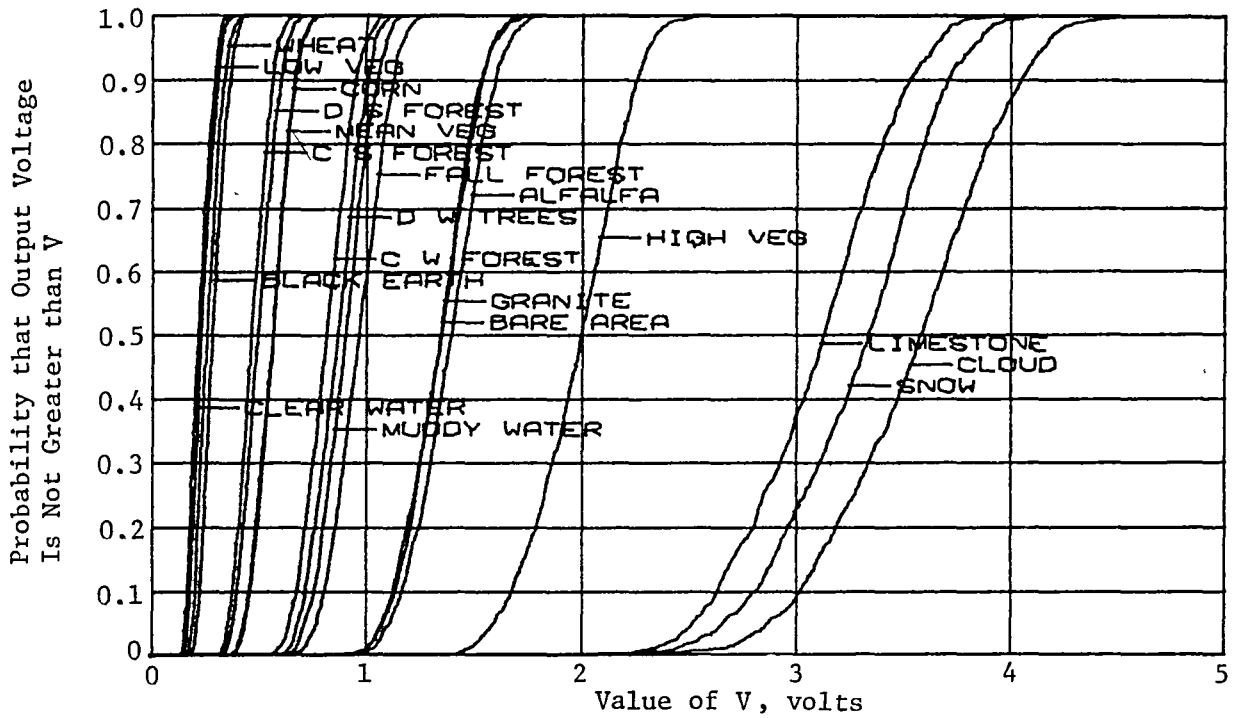


Figure 11 Cumulative Probability Ogives for Fairchild CCD 202 at 23-km Visibility, 0 to 41° Orbit Angle, 650 nm

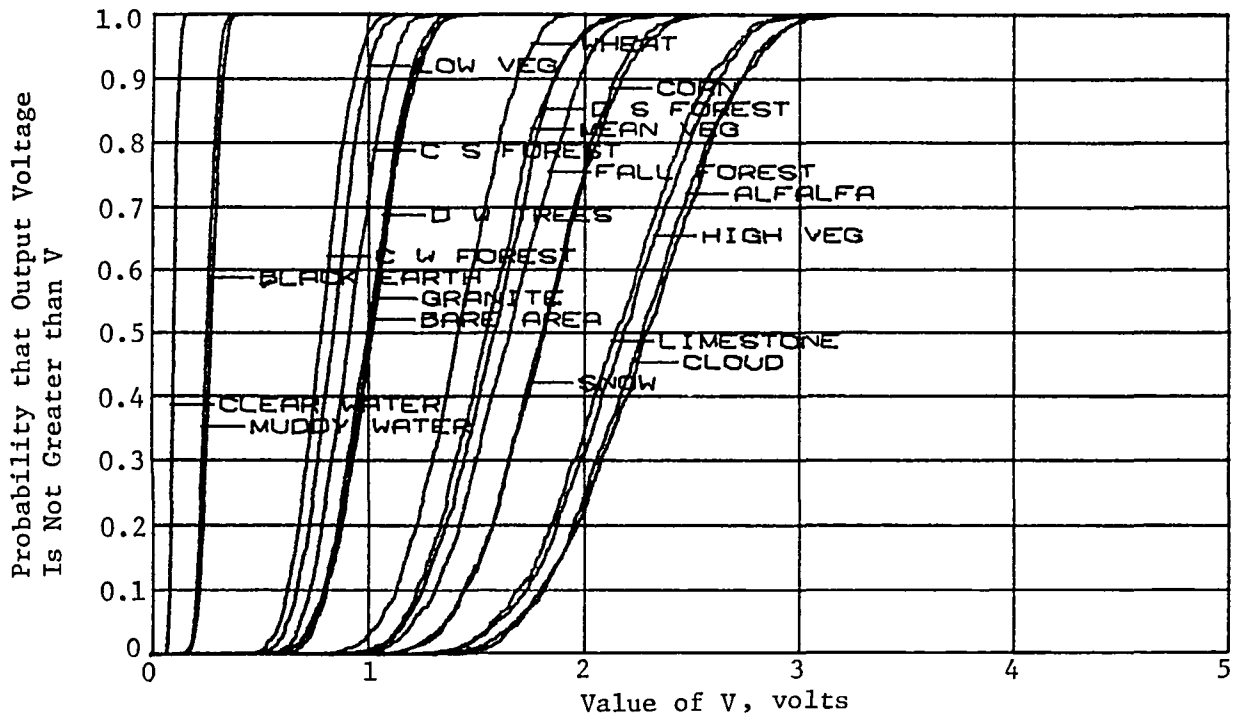


Figure 12 Cumulative Probability Ogives for Fairchild CCD 202 at 5-km Visibility, 41 to 60° Orbit Angle, 850 nm

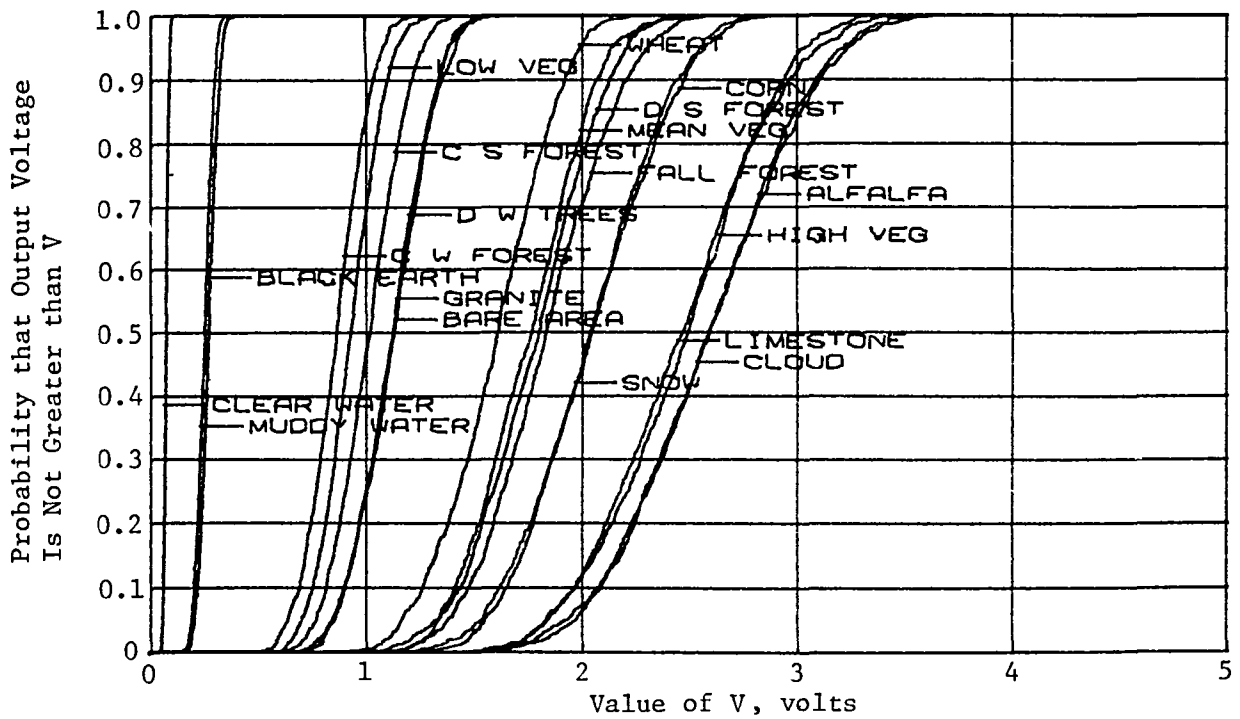


Figure 13 Cumulative Probability Ogives for Fairchild CCD 202 at 23-km Visibility, 41 to 60° Orbit Angle, 850 nm

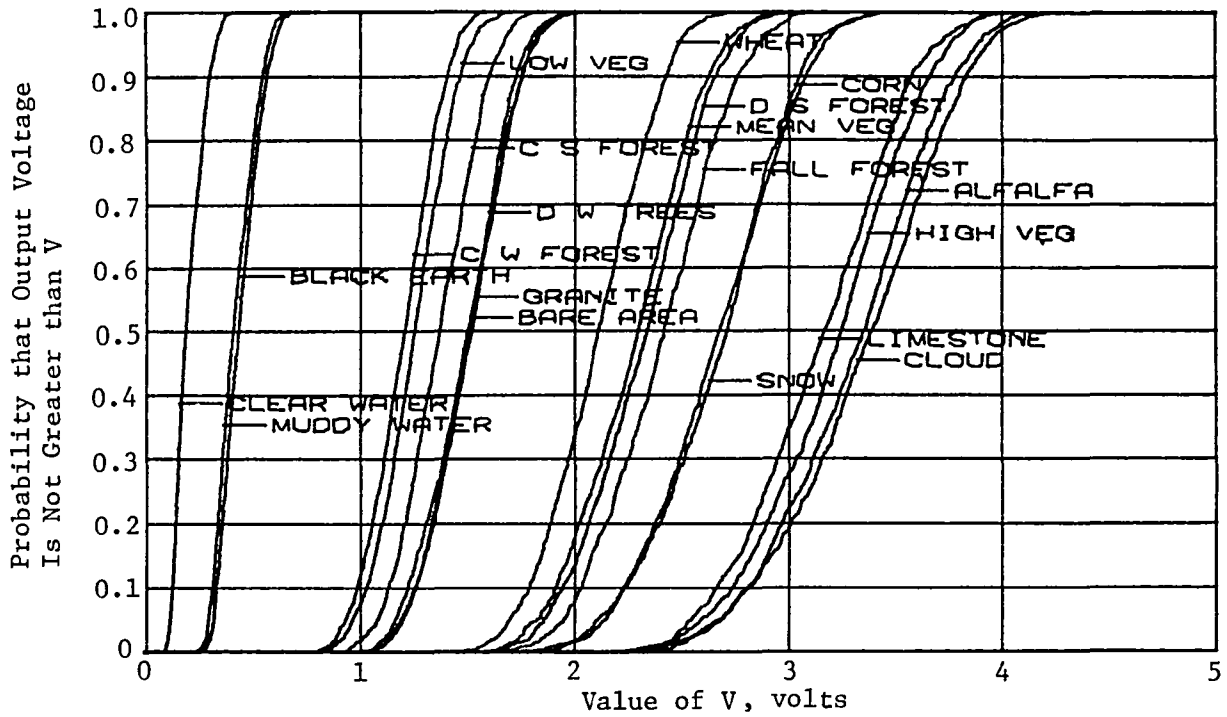


Figure 14 Cumulative Probability Ogives for Fairchild CCD 202 at 5-km Visibility, 0 to 41° Orbit Angle, 850 nm

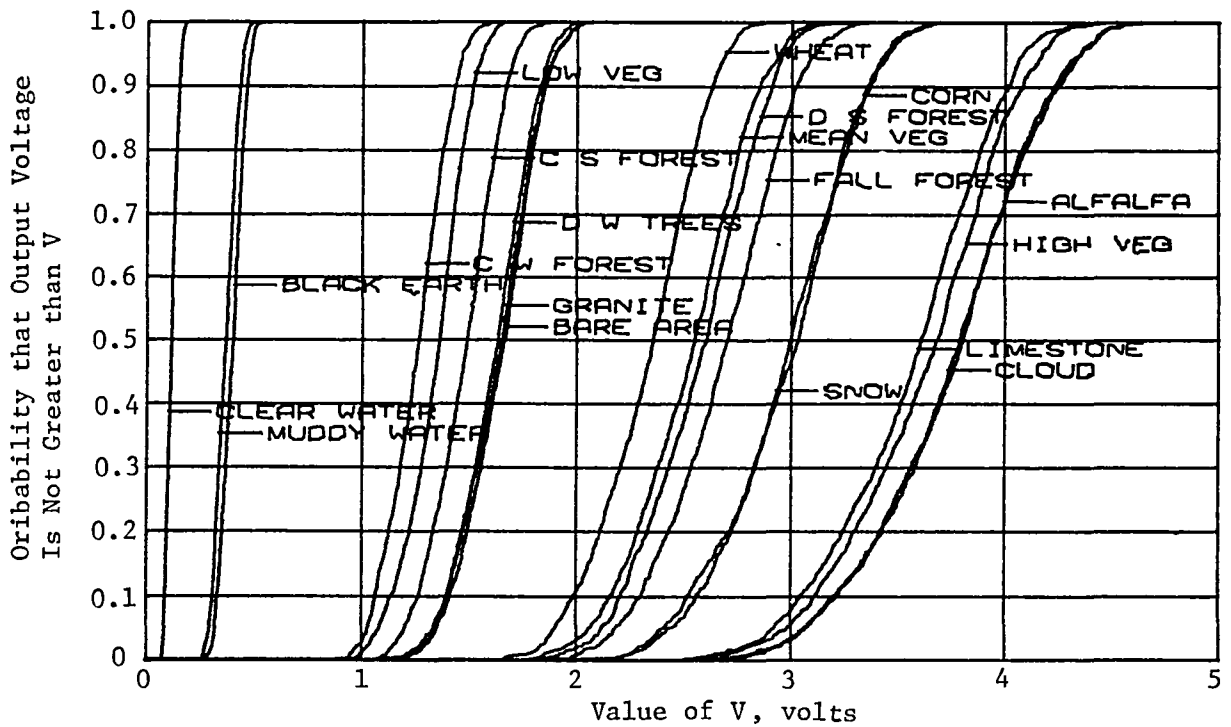


Figure 15 Cumulative Probability Ogives for Fairchild CCD 202 at 23-km Visibility, 0 to 41° Orbit Angle, 850 nm

It was found that separation of bare land and clouds would require some knowledge of the sun elevation, and two ranges were found to be adequate--one threshold could be used with the sun within  $41^\circ$  of zenith and a second could be used when the sun was between  $41^\circ$  and  $60^\circ$  from zenith. When the sun is beyond  $60^\circ$  from zenith, the radiance varies rapidly with sun angle, and extension of FILE operation with such large angles would require relatively precise knowledge of sun position.

From the probability curves, the polygons in Figures 2 and 16 were established. The polygons define the ranges of output voltages from the two FILE TV cameras for the various generic types of features. Three "difficult" features have been ignored in drawing the polygons: (1) limestone (which looks like clouds or snow); (2) black earth; (3) coniferous winter forests. The deletion of limestone is justified by the fact that it represents an extremely difficult case. Even a human observer would find it difficult to distinguish it from clouds or snow on a pixel-by-pixel basis. Black earth is so dark that path radiance dominates, and it therefore would occasionally have a signature that mimics vegetation. Both of these features represent such a small fraction of the Earth's visible surface that special efforts to properly classify them did not appear warranted. Conifer winter forests were deleted because they are a mixture of two categories (snow and vegetation) and therefore do not fit into any single category.

The set of features used to generate the cumulative probability ogives was by no means exhaustive. But it had a wide enough variety of types of vegetation and bare land and water turbidities to establish that a simple instrument can provide useful classification accuracy using only the voltage from one of the cameras and the ratio of the outputs of the two cameras.

The selected decision thresholds are shown superimposed on the polygon plots in Figures 2 and 16. Where the polygons overlap, the decision threshold has been moved a little toward the less common feature to minimize the error rate, as with a Bayesian classifier. However, the relative seriousness of the different possible errors--calling bare land vegetation, calling vegetation cloud, etc--is application-dependent. For an experiment designed to prove a principle with potential for a variety of applications, it made little sense to use a formalized approach because of the subjectivity of any estimate of the seriousness of an error. For a future application in which error costs are readily calculated, it might be reasonable to use, for example, Neyman-Pearson decision logic to set the thresholds. However, greater benefit can probably be derived by adding more comparators, voltage dividers, and logic to the classification circuit, to tailor the decision boundary shapes to the shapes of the polygons, and by reducing the size of the polygons through more accurate estimation of the solar illumination angle.

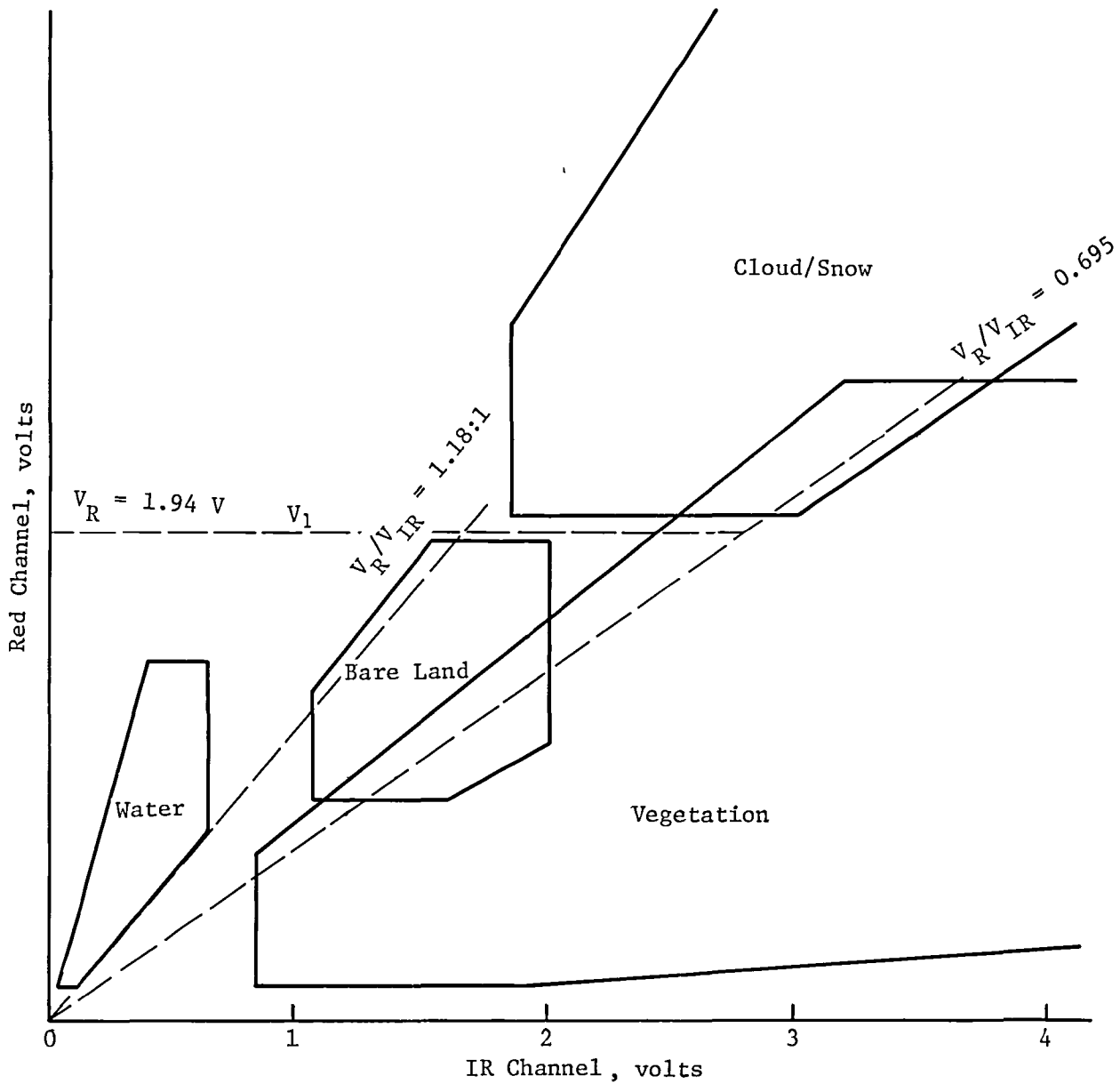


Figure 16 99% Confidence Polygons, Sun 0 to 41° from Zenith

B. FIELD MEASUREMENTS VERSUS ANALYTICAL MODEL RESULTS

Mixed signatures present a potential problem to the FILE approach. If the scene content *within one pixel* is a mixture of cloud and water, FILE may classify it as bare land. Similarly, a mixture of water and vegetation in a pixel might be classed as bare land if the proportions were right--or the latter mixture might be classified as vegetation, even when it was over 50% water, because

of vegetation's higher radiance. Field measurements were therefore taken to determine whether typical real signatures approximated signatures predicted by the analytical model. Two separate trips were taken to obtain data during two seasons.

Summer observations were made with a LANDSAT spectral radiometer, with a 1° field of view. This instrument has two bands that approximate FILE optical filter bands. Channel 1 has response from 580 to 706 nanometers, with a peak between 600 and 650 nanometers, which corresponds to the FILE 650-nanometer band. Channel 2 has response from 767 to 974 nanometers, corresponding to the FILE 850-nanometer band. The LANDSAT bands are wider than FILE bands; but, on the basis of available spectral signatures, the two-band radiance ratio can be expected to be close to the FILE design model radiance ratio. This was found to be the case. Table 3 compares field observations with nominal ratios from the analytical model.

*Table 3  
Comparison of Summer Field Measurements with FILE Design Model*

Feature	Radiance Ratio	
	Ground-Based Field Measurement (Ch 1/Ch 2)	FILE Design Model 650 n mi/850 n mi
Coniferous Summer Forest	0.32-0.382	0.494
Deciduous Summer Forest	0.118-0.201	0.300
Clear Water	2.2	3.29
Clouds	1.51-1.56	1.50
Grass	0.532-0.534	Vegetation High 0.86 Mean 0.308 Low 0.266
Bare Areas	1.22-1.38	1.21-1.41

The winter field trip obtained data on snow and ice. An ERTS radiometer was used to obtain measurements in bands from 600 to 700 nanometers and 800 to 1100 nanometers. Fourteen targets were measured in varying weather conditions, both at Dillon Reservoir and at the Shrine Pass turnoff on Interstate 70 in Colorado.

A pine forest with very little snow gave a radiance ratio of 0.53, compared to 0.494 for the FILE model. Thus, summer and winter observations were found to bracket the value used in the model.

The remaining observations were of snow. They included bright snow (azimuth 150° from the sun), deep snow (azimuth 120° from the sun), and 4-inch snow viewed through blowing snow (azimuth 90° from the sun). Five targets were observed, and all had radiance ratios from 1.58 to 1.63 values, which compare favorably with the FILE model radiance ratio of 1.78.

The ratios agreed well with the FILE model despite the fact that the model is for satellite-based ratios and the bands were somewhat different. Furthermore, the ratios appear to be independent of sun-sensor viewing angles and atmosphere conditions. This fact provides confidence that ground-based tests will be a useful prelaunch check of FILE operation.

### C. ERROR-RATE ANALYSIS

An error-rate analysis was done with the FILE analytical model and the decision thresholds in Figures 2 and 16. The analysis assumed pure targets, i.e., mixtures of types of features within a pixel were not used. The analysis included such factors as orbit position, camera noise, pixel nonuniformity, dark current, atmospheric effects, and viewing angle. The results are shown in Table 4. Because the FILE system estimates the illumination angle on the basis of the time delay from the last sunrise, the analysis modeled a position uncertainty of 1.67° (1σ), with a normal distribution.

Table 4 Classification Errors

Feature	% Called			
	Water	Veg	Cloud	Bare
Cloud	0.0	0.0	100.0	0.0
Wheat	0.0	100.0	0.0	0.0
Low Vegetation	0.0	100.0	0.0	0.0
Corn	0.0	100.0	0.0	0.0
Deciduous Summer Forest	0.0	100.0	0.0	0.0
Mean Vegetation	0.0	100.0	0.0	0.0
Coniferous Summer Forest	0.0	100.0	0.0	0.0
Fall Forest	0.0	100.0	0.0	0.0
Alfalfa	0.0	100.0	0.0	0.0
Deciduous Winter Forest	0.0	97.1	0.0	2.9
High Vegetation	0.0	100.0	0.0	0.0
Coniferous Winter Forest	0.0	65.5	0.0	34.5
Black Earth	1.0	8.9	0.0	90.1
Granite	0.0	0.7	0.2	99.1
Bare Area	0.0	0.6	0.0	99.4
Limestone	0.0	0.0	100.0	0.0
Snow	0.0	0.0	100.0	0.0
Clear Water	100.0	0.0	0.0	0.0
Muddy Water	100.0	0.0	0.0	0.0

As expected, the highest error rates are for winter scenes-- mixtures of snow with vegetation--and limestone and black earth. For many feature types, the error rate was essentially zero.

#### D. DATA-TAKING INTERVAL ANALYSIS

The last FILE analysis to be described was to determine how often the FILE system should be activated to give a high degree of confidence that the full data-storage capacity would be used while providing good variety in the collected data. For this analysis, a map of the world was entered in the computer. The map was divided into cells of 5° latitude by 5° of longitude, and a scene class--water, bare land, or vegetation--was assigned to each cell as shown in Figure 17.

Clouds were then randomly superimposed on the map and a simulated mission was "flown" over the map with the OFT-2 reference flight profile orbit. Each time the simulation indicated that the FILE system would attempt to take data, latitude and longitude were calculated and used to look up the "scene class" on the map. Where the scene class was bare land, water, or cloud, the corresponding scene class counter was checked and incremented. If the counter had not reached a full count--or if the scene was vegetation--a "picture" was taken. The simulation kept track of the number of pictures taken versus time.

A total of 200 simulated missions were run for each analysis so that statistics could be compiled. The selected 2.75-minute picture-taking interval was established by iterating the analysis for different intervals.

Three separate cloud models were used, and all three gave similar results. In one model, a random number was assigned to each cell on the map. A "slicing threshold" value was then adjusted so that half the cells had random numbers above the threshold and half had numbers below it. Cells with numbers above the threshold were then labeled cloud cells. In another model, the random numbers were averaged with adjacent cells before the slicing threshold was applied. This generated larger clouds and larger areas where the ground was visible. In the third model, the averaging with adjacent cells was done twice. This produced supercontinental-sized clouds. Figures 18, 19, and 20 show typical cloud patterns with these models.

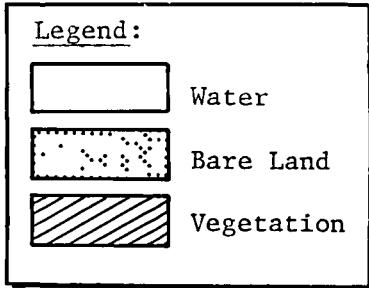
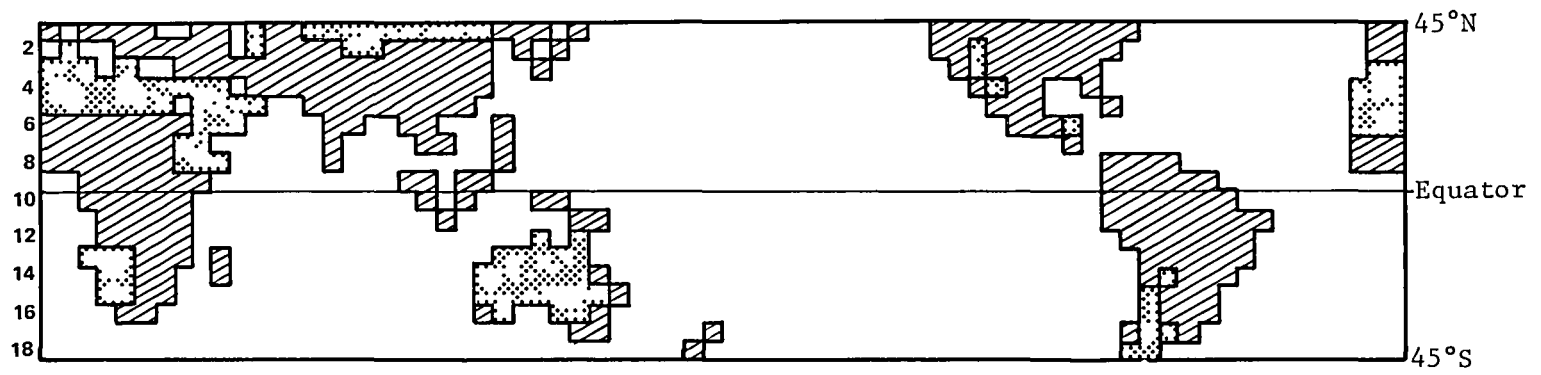


Figure 17 World Map (without clouds)

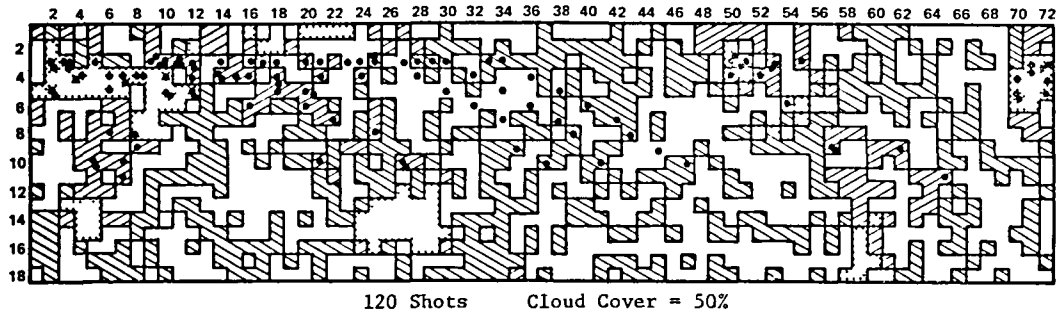


Figure 18 Small Cloud Model (typical run)

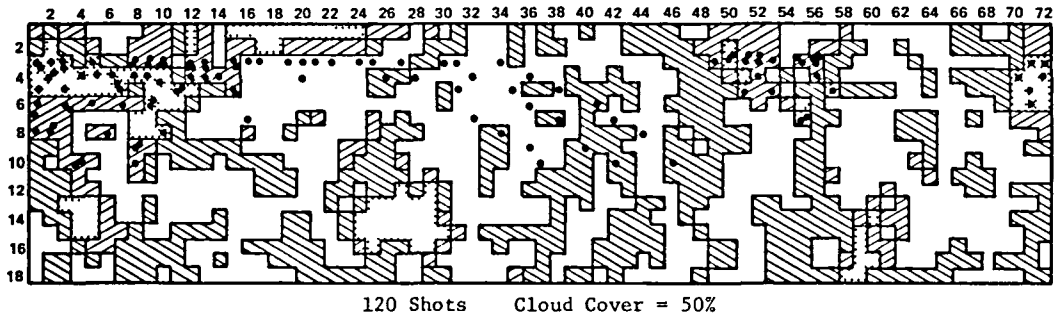


Figure 19 Medium Cloud Model (typical run)

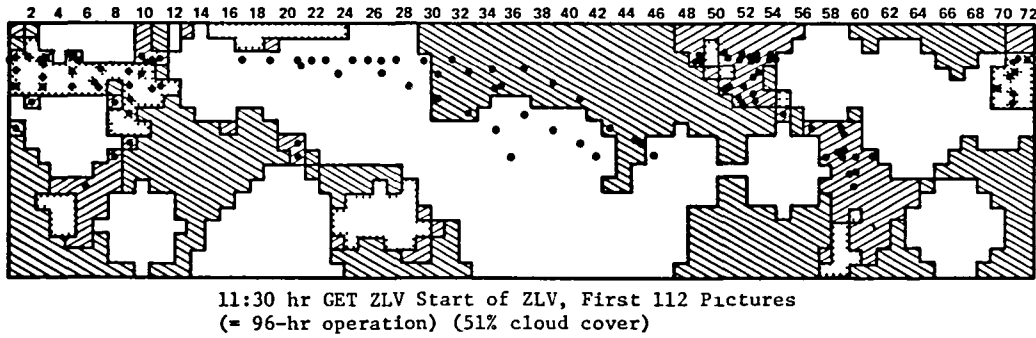
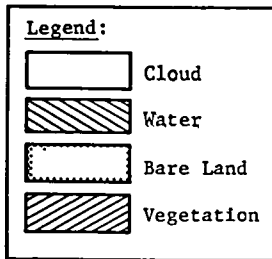


Figure 20 Large Cloud Model (typical run)



With the 2.75-minute interval, the following results were found to be typical for any cloud model:

- 1) The best case produced 120 pictures in 35.4 hours;
- 2) The worst case produced only 85 pictures in 96 hours -
  - a) 32 bare land (full limit),
  - b) 21 vegetation and mixed signature,
  - c) 11 all water,
  - d) 21 clouds;
- 3) Half the simulated missions ran 63.7 hours or less to get 120 frames of data;
- 4) 77.5% of the missions produced 120 frames of data in less than 84 hours;
- 5) 12% did not produce 120 pictures in 96 hours;
- 6) Typically, 54.9 to 80.3 hours were required to get 120 frames of data.

This simulation was based on a 96-hour ZLV period. Because it now appears that the actual first flight of FILE will allow as little as 65 hours for data taking, it would be wise to rerun this analysis when actual mission parameters are established.

One interesting finding from the simulation was that data taking was concentrated in the most northern latitudes because these latitudes have the most favorable sun angles in the summer and because the rate of change of latitude with time is less at latitude extremes than near the equator. Therefore the results of this analysis are only valid for a summer mission. For a winter mission, data-taking will be concentrated in the southern hemisphere where there is less land. A winter mission can therefore be expected to require a shorter data-taking interval. On this basis, it is recommended that the analysis be repeated for any significant change in launch date.

V. ADVANCED FILE CONCEPT

---

A. COASTLINE TRACKING ALGORITHM

A coastline tracking algorithm was developed under a previous contract and reported in Reference 1. Under the current contract, analysis of this algorithm was expanded to include noise effects and error rate analysis. For the benefit of the reader who is not already familiar with this algorithm, the previously published description is repeated here.

1. Algorithm Description

If a television camera scans a circular pattern over a high-contrast edge in an image as shown in Figure 21, the video signal will be (to a first approximation) a periodic square wave of the same frequency as the scanning rate. Scanning is accomplished by adding a voltage  $V_x = V_m \sin(\omega t)$  to the vertical deflection voltage, and  $V_y = V_m \cos(\omega t)$  to the horizontal deflection voltage, where  $V_m$  is much less than the deflection voltage required to cover the width of the sensor field of view.

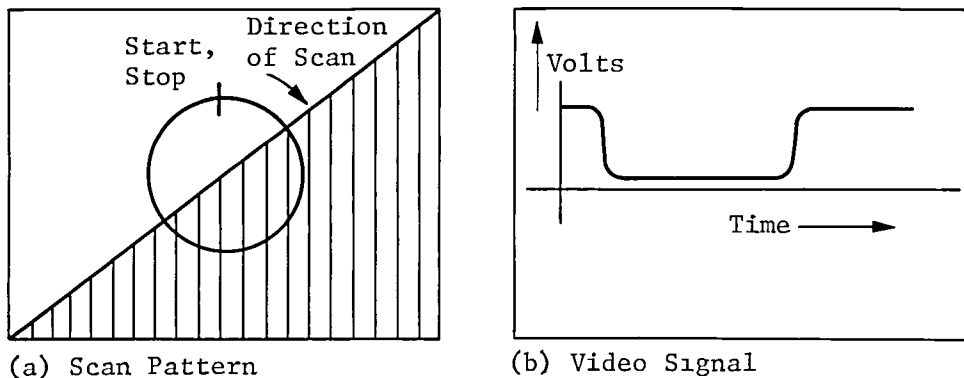


Figure 21 Scan Configuration

If the fundamental-frequency sine and cosine coefficients of the Fourier series expansion of the video signal are interpreted as the horizontal and vertical components of a vector, the vector is found to be perpendicular to the edge and pointing toward the brighter side of the edge. Vector length is greatest for sharp

high-contrast edges and has maximum length when the circle is centered on the edge. If vector length is divided by the video signal dc component, the result is essentially independent of scene brightness.

Required coefficients are readily found with the circuitry in Figure 22, which uses analog computer techniques to directly compute the Fourier coefficients:

$$a_0 = \frac{\omega}{\pi} \int_0^{2\pi/\omega} f(t) dt \quad [1]$$

$$a_1 = \frac{\omega}{\pi} \int_0^{2\pi/\omega} f(t) \cos(\omega t) dt \quad [2]$$

$$b_1 = \frac{\omega}{\pi} \int_0^{2\pi/\omega} f(t) \sin(\omega t) dt. \quad [3]$$

The circuitry can be used to seek a coastline by sweeping the center of the circle back and forth across the middle of the image on the camera photocathode at a rate much slower than the circular scanning. If the largest normalized vector length  $\sqrt{b_1^2 + a_1^2}/a_0$  is greater than 0.22, a high-contrast sharp discontinuity has been found, and the tracker switches from acquisition mode to tracking mode.

In the tracking mode, the circle is displaced on the photo-cathode after each decision, starting at the position with maximum normalized vector length as found above. Decisions are made by the following algorithm, which may be implemented with analog or digital electronics or with an on-board computer, if one is provided for other functions. In the algorithm, the "y" direction is assumed to be in the direction of satellite travel, and  $x_0$  and  $y_0$  are voltages to position the scanning. Initially, scanning is positioned at the point determined above. The following steps are then followed:

- 1) Clear flip-flop A. This flip-flop passes  $a_1$  and  $b_1$  when cleared but multiplies them by -1.0 when it is set;
- 2) Let  $\ell = \sqrt{a_1^2 + b_1^2}$  (this can be computed with analog circuitry if this is most convenient in the particular system);

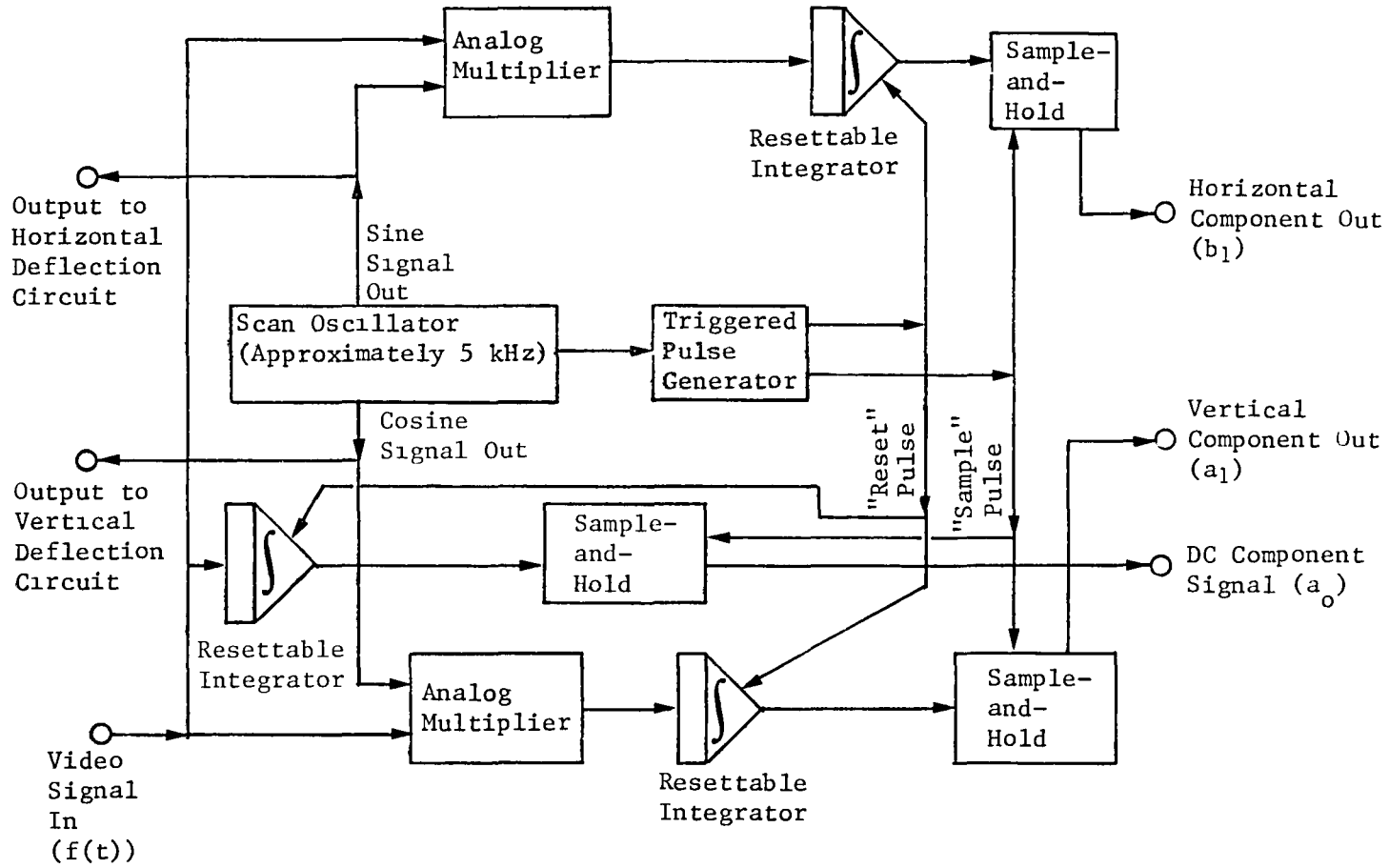


Figure 22 Circuitry for Computing Vector Components

- 3) If  $a_1$  is greater than zero, the system will be tracking in the opposite direction from the satellite's motion, so set flip-flop A to reverse the polarity of  $a_1$  and  $b_1$ ;
- 4) Let  $\Delta y = -a_1 k/\ell$ , where  $k$  is a gain factor selected for best system performance, chosen during equipment design so that  $\sqrt{(\Delta y)^2 + (\Delta x)^2}$  is a fraction of the circle radius;
- 5) Let  $\Delta x = -b_1 k/\ell$ ;
- 6) Let  $d_x = \Delta y$ ;
- 7) Let  $d_y = \Delta x$ ;
- 8) Scan circles centered at  $(x_1 = x_0 + d_x + \Delta x, y_1 = y_0 + d_y + \Delta y)$ ,  $(x_2 = x_0 + \Delta x, y_2 = y_0 + \Delta y)$ , and  $(x_3 = x_0 - d_x + \Delta x, y_3 = y_0 + d_y + \Delta y)$ , and determine new Fourier coefficients for each. The centering producing the maximum value of  $\sqrt{(a_1')^2 + (b_1')^2}/(a_0')$  is taken as the new  $(x_0, y_0)$ , and  $a_1, b_1, a_0$ , and  $\ell$  now become the values for this centering.
- 9) If the procedure has not caused tracking off the photocathode and  $\ell/a_0 > 0.22$ , go to step 4;
- 10) Otherwise, return to acquisition mode.

Drift in analog circuits can be tolerated if an analog approach is used to implement the algorithm, because the procedure is self-correcting with reasonable drift rates. Correction for satellite motion is required if a very narrow field of view is used.

The high-resolution camera is positioned by the tracking camera voltages  $x_0$  and  $y_0$  in the preceding algorithm. Pictures are taken periodically when the system is in the tracking mode. This should produce a high percentage of coastline and river photographs.

## 2. Cloud Detection

A sharp contrasting edge is not necessarily a coastline. The edge might be the boundary between forest and bare rock or soil, between irrigated land and desert, between cloud and land, or between cloud and water. To be most useful, the algorithm should distinguish between shorelines and other types of edges.

One solution to this problem involves restricting the spectrum the camera "sees" to a part of the spectrum where coastlines tend to produce vectors much longer or much shorter than other edges. Deep red appears to be the best part of the spectrum for this.

For example, at 750 nanometers, the reflectances of coniferous forest and granite are very nearly the same, so the "vector" produced by the edge between these two types of terrain would be quite short. However, water has very little reflectance at this wavelength, and a water-granite or water-forest interface would produce a long vector.

Unfortunately, interfaces between clouds and nearly all types of terrain would also produce long vectors, as shown in Figure 23.

At a single wavelength, a cloud-land interface might produce a vector length very much like that produced by a land-water interface. The confusion can be resolved by computing the vector length again at, for example, 470 nanometers where a land-water edge would typically produce a shorter vector--in some cases even opposite in direction--while a cloud-land vector would tend to be near the same length at both wavelengths or actually be longer at the shorter wavelengths, as illustrated in Figure 24.

Because the algorithm requires a wide but not particularly long cathode in the direction of satellite motion, this two-color measurement might be done with one camera. One half of the photocathode would be used for a scene filtered for 470 nanometers. The other half would be used for the same image filtered for about 750 nanometers. This arrangement is illustrated in Figure 25. If a dual-aperture image-dissector camera were used, the electronics package could simply switch in whichever image was desired or process both in parallel.

A complete description of a tracker of this type is given in Reference 1 along with a discussion of the suitability of microprocessors for use in a tracker of this type.

A laboratory experiment was conducted with a simulated cloud and a gelatin filter to verify that vector length changes in the expected manner with filtering. Experimental results agreed with predicted results, in which vector length was changed over a 2.8:1 range by filtering.

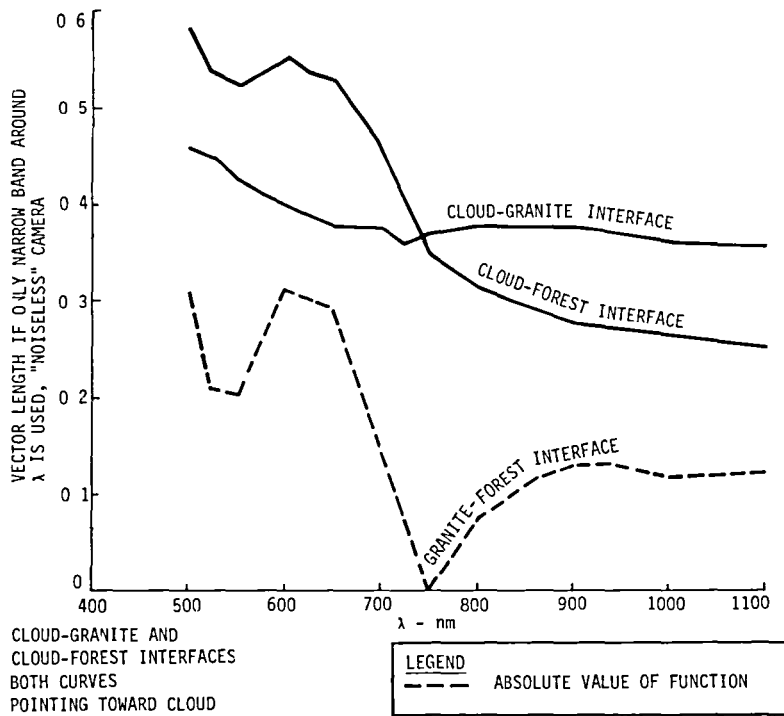
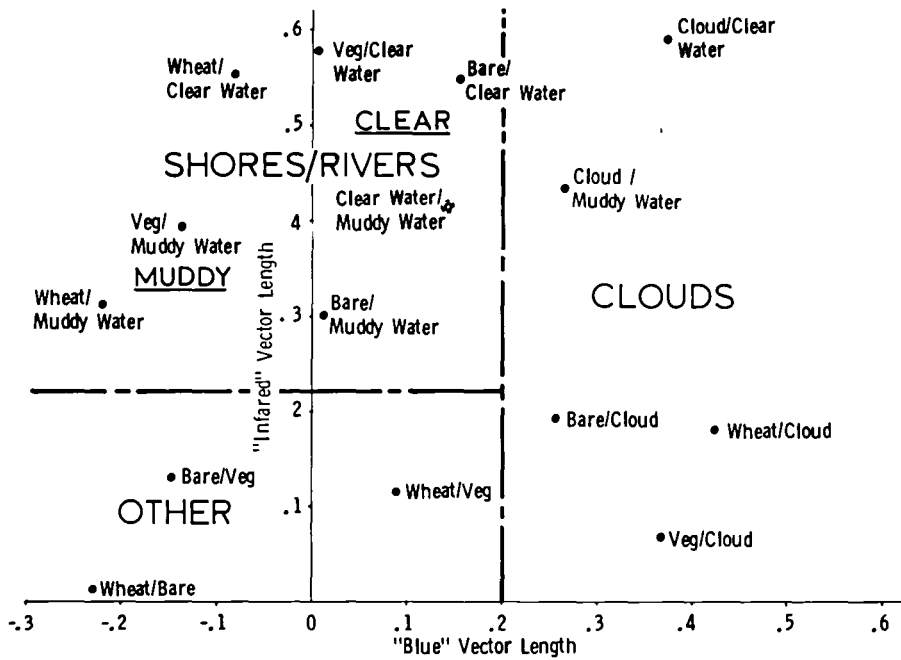


Figure 23  
 Vector Length as a Function of Wavelength for Various Interfaces



(Negative Value Indicates Polarity Opposite of Infrared Vector's Polarity)

Figure 24  
 Blue/Infrared Vector Pairs for Various Interfaces

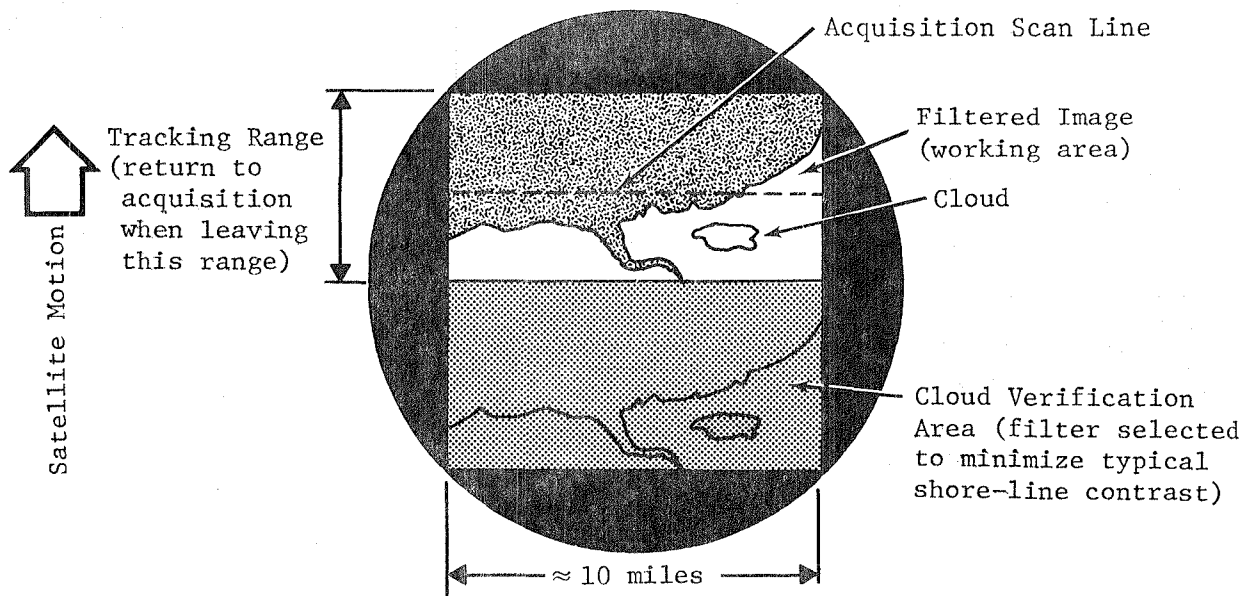


Figure 25 Image on Photocathode for Two-Band Scanning

The second approach to cloud detection requires more sophisticated electronics but simpler optics. It is based on the fact that, compared to land, clouds and water both tend to appear very smooth at 750 nanometers. If the electronics package compares the ratio of ac component to dc component in the video signal on the "dark" side of the edge with that on the "bright" side, clouds might be recognized because the bright side in this case has less granularity. This approach shows somewhat less promise than the multifilter approach described, but it would be smaller and lighter in weight. Laboratory experiments have not been conducted to test the second method; however, analysis indicates that it would be more apt to make errors than the other method. Good results might be obtained by combining the two techniques.

*Experimental Results* - The tracking algorithm has been tested. Figure 26 was produced by a PDP-9 computer from Figure 27 by implementing the algorithm with an image dissector camera and using an analog/digital interface to allow the computer to simulate the functions of some of the electronics. The computer produces a line-printer plot of the scene, then, with a chart recorder, traces on the plot the path it tracked, for a permanent record of the run. The scene used was a satellite photograph, as shown in Figure 27. To the scale of these images, the "scanning circle" diameter was approximately 6.8 millimeters (0.27 in.).



In this experiment, there were no confusion factors such as clouds or high-contrast features other than coastlines, and no islands were encountered. More experiments were run to see what would happen when these factors were introduced. It was found that clouds over land were not frequently mistaken for coasts. This was probably largely due to chance and to the fact that the clouds were small with respect to the scanning circle. In one experiment, tracking proceeded normally until a coastal cloud was encountered. Tracking then went around the cloud until the satellite motion (simulated by computer software) moved the cloud out of the field of view. The algorithm then relocated the coast and continued tracking properly. Similar problems have been encountered with islands. The latter should be a minor problem in a real satellite because the content of the field of view completely changes approximately once every 1.2 seconds, representing about 9 kilometers (6 mi) of satellite motion. This would automatically prevent continuous circling of the island. Analysis indicates that the clouds could be avoided by one or both of the cloud detection techniques described earlier.

The minimum vector length for tracking in step 7 of the algorithm on page 33 was determined experimentally. Real coastlines in the pictures used produced vector lengths on the order of 0.25, and few other features produced lengths over 0.10. When the threshold was set to zero, the tracker wandered randomly over the photograph after coming to the end of a river. When the tracker again encountered a coast, it went back to tracking the coast properly. Where picture brightness increased or decreased as a function of distance from the coast, the tracker tended to track a constant-brightness contour parallel to the coast for a considerable distance. The experiment used a threshold of 0.14 to track a feature and 0.03 to cause a return to the acquisition mode. A wide range of threshold settings between 0.03 and 0.25 seem to work well. The optimum setting is difficult to determine using photographs because it depends on what optical filtering is used and perhaps on sun angle and other factors. The maximum possible length is 0.6366.

### 3. Recent Studies

Under the current contract, the above experiments were expanded to include investigation of error rates and related parameters for such a system implemented with an image-dissector camera. The results of this investigation indicate that the conceptual simplicity of using the image dissector's random scan capability and essentially instantaneous response are offset by speed limitations caused by shot noise and photocathode degradation.

*Tracking Angle and Vector Length Errors* - Shot noise is one factor limiting the performance of a coastline tracker based on an image dissector. The noise will produce errors in both tracking direction and tracking "vector" length. The former will cause the system to leave the land-water boundary. The latter could cause the system to abandon tracking altogether because the interface does not appear to have the contrast of a land-water boundary.

To evaluate the effect of noise, a camera noise model that used a random-number generator was devised. The model included Poisson-distributed shot noise simulating the front end of the camera tube followed by a log-normal random-gain model for the photomultiplier.

For analysis of tracking-angle error, the scanning circle was divided into 157 discrete steps and a noise-corrupted current sample was generated for each step. The phase shift from amplifier roll-off and dark current were also modeled. Amplifier noise was found to be insignificant compared to that from the photomultiplier, and was ignored.

Figure 28 shows how the tracking angle varies with photocathode emission from the bright side of a simulated 90% contrast boundary. The analysis assumed a 5-kilohertz scanning rate, amplifier roll-off at 250 kilohertz, and a 25.4- $\mu$  (1-mil) diameter round scanning aperture. The graph indicates that current densities above about 1  $\mu\text{A}/\text{cm}^2$  can be expected to provide fairly good tracking performance. Because current densities up to about 8.2  $\mu\text{A}/\text{cm}^2$  can be used with reasonable (6-year) camera life, tracking angle error caused by noise does not appear to be a significant problem. To verify this for lower contrast boundaries, the analysis was rerun for a range of contrasts. The results are presented in Figure 29. The simulated electronics and scan rate were the same as in the previous analysis.

As the figure shows, the tracking angle error is not greatly affected by the boundary contrast if contrast is above about 50%. Because tracking will always be on a high-contrast edge, it does not appear that tracking accuracy is a problem.

Vector length is used for recentering the scanning circle on the land-water boundary and to distinguish land-water boundaries from cloud-land or cloud-water boundaries.

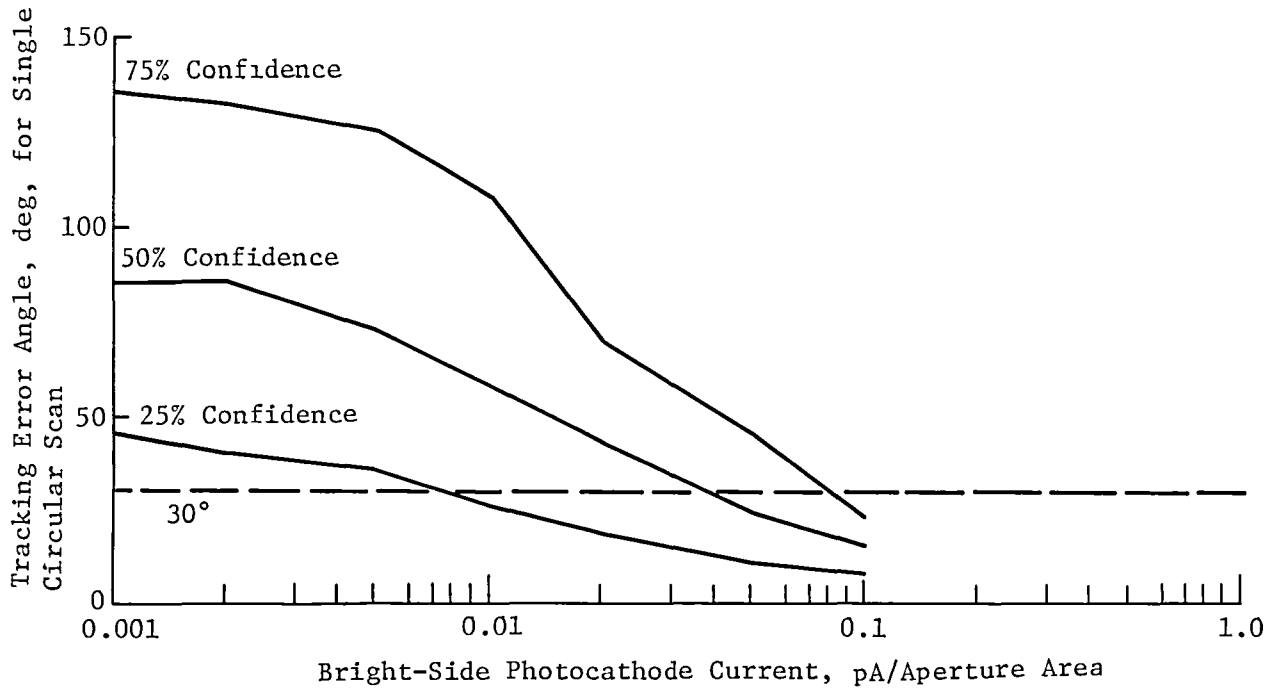


Figure 28 Tracking Angle versus Photocathode Emission

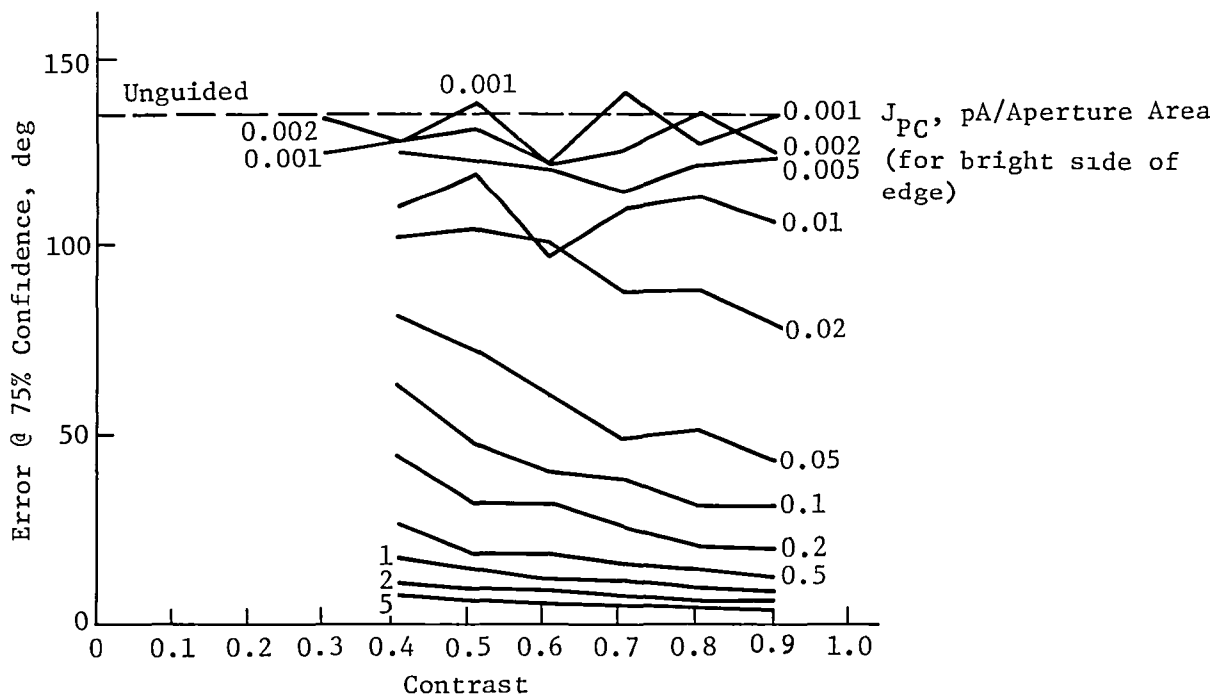


Figure 29 Error Angle versus Contrast for Various Current Densities

An error in determining the vector length could cause the instrument to stop tracking a true land-water interface either because it appeared to involve a cloud or because the interface appeared to have insufficient contrast for a coastline. Accuracy in determining the vector length is therefore required to minimize errors in track/don't track decisions.

The same camera model was used to determine how measured vector length varies with true vector length (which is a function only of contrast) and photocathode current density. The results of this analysis are presented in Figure 30. Again, indicated current densities are for the bright side of the interface, and a 5-kilohertz scan rate is assumed.

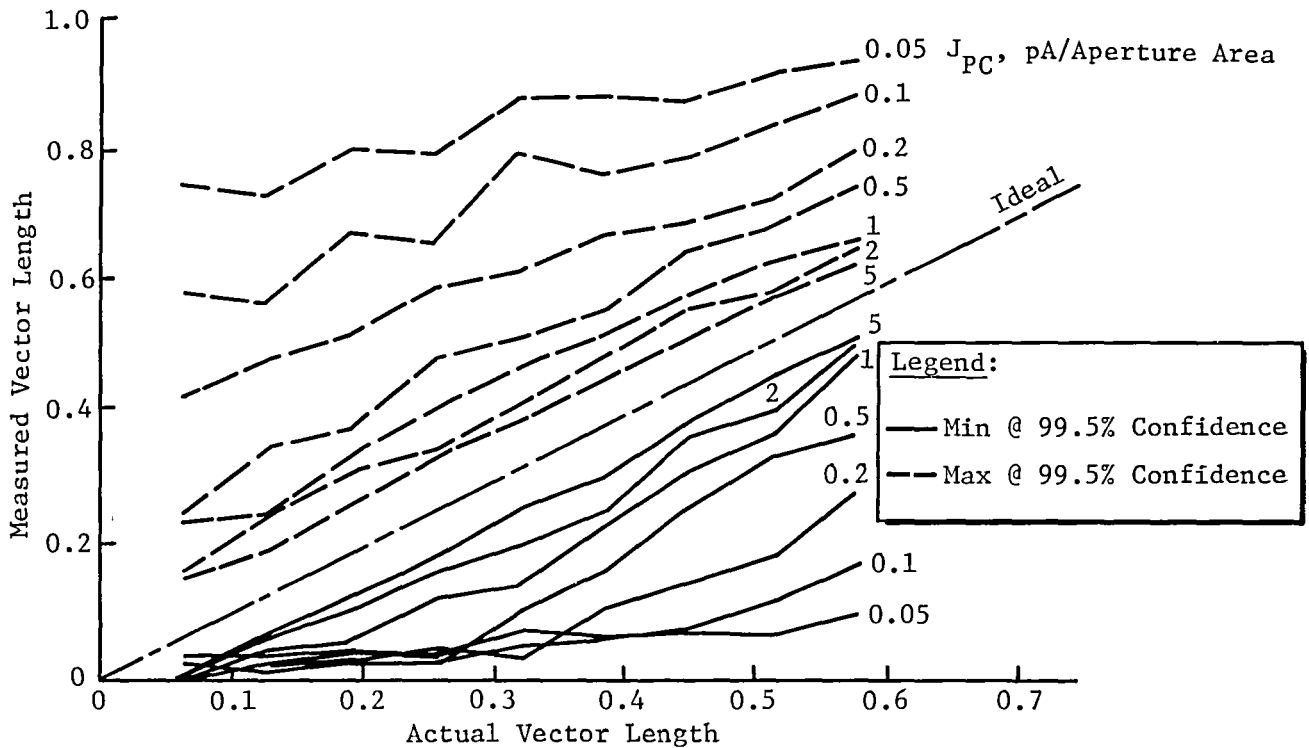


Figure 30  
 99.5% Confidence Limits for Observed Vector Length versus  
 True Vector Length at Various Current Densities

It appears that using the 5-kilohertz scan rate with this camera results in marginal operation, even with a current of 5 picoamperes through the aperture. The range for acceptable operation is on the order of 5 to 50 picoamperes; at the latter current density, photocathode life would be about 1½ months--far too short for most space applications. However, the effect of higher photocathode current density can also be obtained by using a lower scanning rate. In general,

to multiply effective current density (from a noise standpoint) by a given factor, the scan rate must be reduced by a comparable factor. Figure 31 shows how the standard deviation of the observed vector length varies with photocathode current density and scan rate for a 90% contrast interface.

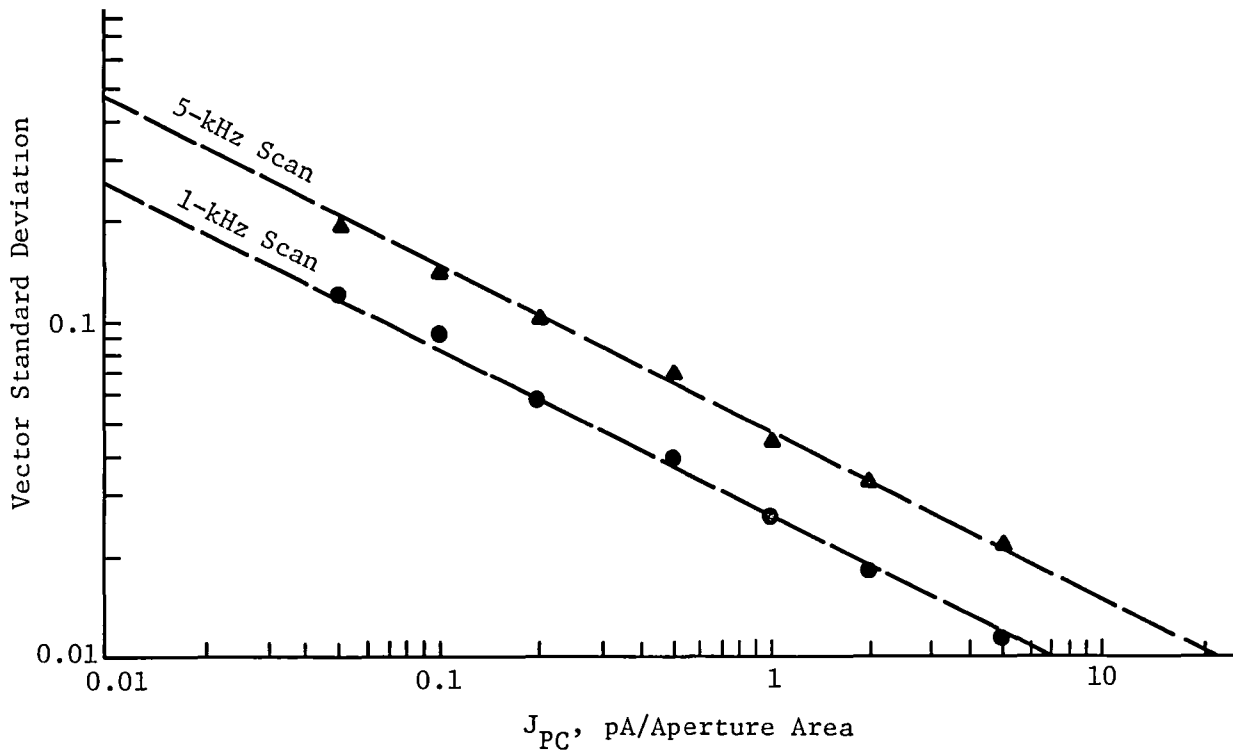


Figure 31  
Vector Standard Deviation versus Photocathode Current Density for Two Scan Rates

The results of this investigation suggest that the practical range of scanning frequency is about 200 to 1000 hertz, and the required photocathode current density is on the order of 16 to 80  $\mu\text{A}/\text{cm}^2$  for an image dissector with a 25.4- $\mu$  diameter. A Monte Carlo analysis was done to determine the probability of misclassifying a boundary. All interfaces of clouds, bare land, wheat, muddy water, clear water, and average vegetation were simulated with a scan rate of 1000 hertz and bright-side photocathode current densities of 40 and 80  $\mu\text{A}/\text{cm}^2$ . With the lower current density, the simulated system made errors about 5% of the time with each of the three interfaces. It occasionally classified an interface of bare land or wheat with clear water as a cloud edge, and occasionally accepted an area of clear water with no interface at all as a legitimate coastline. The reason for the latter appears to be that the signal level was so low, because of the low reflectance of the water, that the noise became a primary factor in determining vector length.

When the higher current density was used, the system made only one error in 420 scans. Again this was the acceptance of an area of clear water as a legitimate coastline. It appears that additional logic could easily be added to reflect any interface with an average camera output below a certain level, and that this would cure the problem. Even the higher current density can be achieved with standard optics and does not present a difficult lens design problem.

The relatively high photocathode current densities required and narrow operating range allowed by the competing factors of photocathode life and noise reduce the overwhelming advantages that were once thought to exist in using an image dissector. Moreover, the problem identified above, in which the system occasionally accepts water as a coastline, is readily avoided with direct recognition of feature types on a pixel-by-pixel basis as is done in the Feature Identification and Location Experiment (Ref 2).

## B. RECOMMENDED IMPLEMENTATION FOR SURFACE-FEATURE TRACKING

Recently it has been shown that competing tracking technologies such as CCDs offer advantages in terms of life and performance. The scanning rate limitations imposed by the factors investigated bring the operating speed of an image dissector down to the range achievable with solid-state sensors. Other factors recommending solid-state sensors include: (1) solid-state cameras are, in general, less expensive than alternative sensors; (2) CCD technology is still improving while significant improvements in image dissectors appear less likely; (3) FILE I preprocessing provides a convenient way to distinguish coastlines from cloud boundaries without added logic, (4) part of the FILE I design can be reused; and (5) CCDs do not present high-voltage problems.

However, a CCD does not have a random scan capability. The pixels must be scanned in a predefined order and at a constant rate. Moreover, all pixels in the frame must be scanned each frame whether they are used or not. Implementation of the circular scan algorithm with CCDs will therefore involve a scene memory and predominantly digital operations as opposed to the analog operations of the original concept. Also the scanning circles can only be approximated because the CCDs have discrete picture elements.

Because of the large amount of digital hardware required for a random-logic implementation, and because it is desirable to make the system flexible and expandable, a general-purpose digital signal processor running from a program in memory looks attractive. Martin Marietta has been designing and analyzing such a processor based on the Advanced Micro Devices 2900 chip set. The microcode for such a processor can be used to generate control signals to operate dedicated random-logic portions of the instrument and, where speed is not a limitation, it can replace random logic.

A program has been written to verify that a processor of this type operates fast enough to keep up with the CCD scan rate. It appears from this benchmark program and the current design concept that iteration rates on the order of 1000 per second can be handled. These rates are comparable to the capability of an image dissector system. Moreover, the flexibility of the processor allows this rate to be tailored to the requirements of the external sensor or mount being controlled.

This design allows for addition of features such as area correlation for recognition of specific landmarks, registration, other tracking modes, navigational update functions, and additional sensors whose formats and fields of view may differ from the CCDs' (e.g., IR sensors), without major effects on circuit design. In short, the system is being designed with incremental expansion in view.

A bit-slice architecture was selected to provide software compatibility with the PDP 11/45 FILE simulation computer. This architecture permits emulation of popular processors while maintaining a fast instruction execution time.

The VILAT processor has eight general-purpose registers and eight addressing modes to permit the programmer to select the precise instruction needed for a specific operation. Addressing modes include sequential forward or backward addressing, indexing, indirect addressing, and stack addressing. The eight general-purpose registers are not dedicated to specific functions. They can be used as accumulators, index pointers, sequential pointers, or as index registers.

The VILAT processor uses device registers for input and output. Because the device registers can be manipulated by the processor as flexibly as memory, instructions that manipulate data in memory can be used equally well to transfer data to and from peripheral devices. The VILAT processor will implement only a basic subset of the PDP 11/45 instruction set. Table 5 lists the instruction set for the VILAT processor.

Figure 32 is a detailed block diagram of the VILAT processor. Figures 33 through 40 are logic diagrams for each function block. The scene processor block is for future expansion, to provide registration capabilities. Special instructions for manipulating the scene processor can be added to the processor instruction set as needed.

Table 5 VILAT Processor Instruction Set

Mnemonic	Description
CLR	Clear register or memory location
COM	Complement (1s) register or memory location
INC	Increment register or memory location
DEC	Decrement register or memory location
NEG	Complement (2s) register or memory location
TST	Test register or memory location
ROR	Rotate right register or memory location
ROL	Rotate left register or memory location
ASR	Arithmetic shift right register or memory location
ASL	Arithmetic shift left register or memory location
ADC	Add carry to register or memory location
SBC	Subtract carry from register or memory location
SXT	Sign extend register or memory location
MOV	Move register to register, register to memory location, or memory location to register
CMP	Compare register to register or register to memory location
ADD	Add registers, register and memory location, or memory locations
SUB	Subtract registers, register and memory location, or memory locations
BIT	Bit test (AND) registers, register and memory location, or memory locations
BIC	Bit clear (A · B) registers, register and memory location or memory locations
BIS	Bit set (OR) registers, register and memory location, or memory locations
XOR	Exclusive OR registers, register and memory location, or memory locations
BR	Unconditional branch
BNE	Branch if not equal zero
BEQ	Branch if equal to zero
BPL	Branch if plus (or zero)
BMI	Branch if minus
BVC	Branch if overflow clear
BVS	Branch if overflow set
BCC	Branch if carry clear
BCS	Branch if carry set
JMP	Unconditional jump
JSR	Jump to subroutine
RTS	Return from subroutine
MARK	Mark (aid in subroutine return)
HALT	Halt
NOP	No operation
CLC	Clear carry status bit
CLV	Clear over-range status bit
CLZ	Clear zero status bit
CLN	Clear negative status bit
CCC	Clear all status bits
SEC	Set carry status bit
SEV	Set over-range status bit
SEZ	Set zero status bit
SEN	Set negative status bit
SCC	Set all status bits

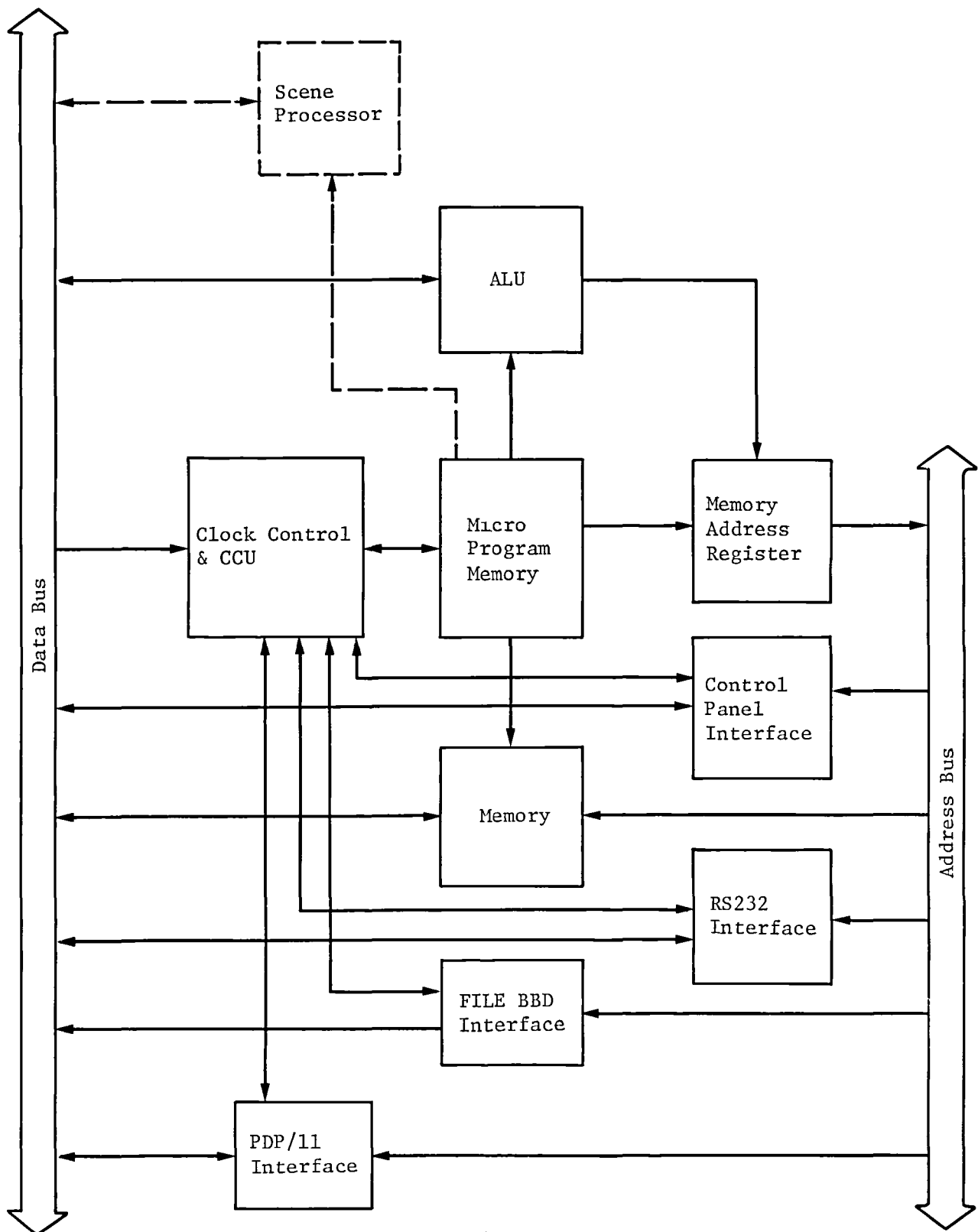


Figure 32 VILAT Processor Block Diagram

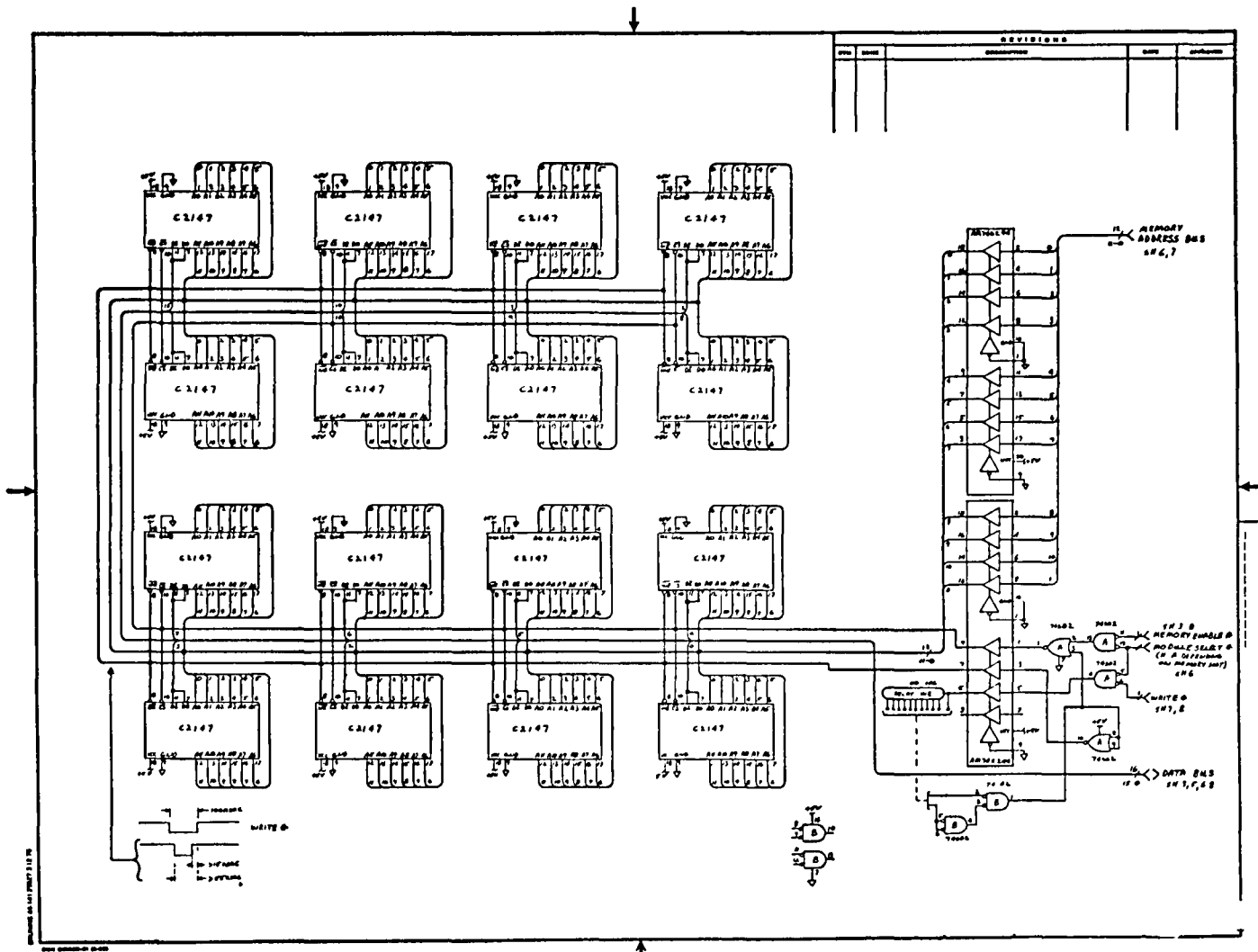


Figure 33 VILAT Processor 4K Memory Module Logic Diagram



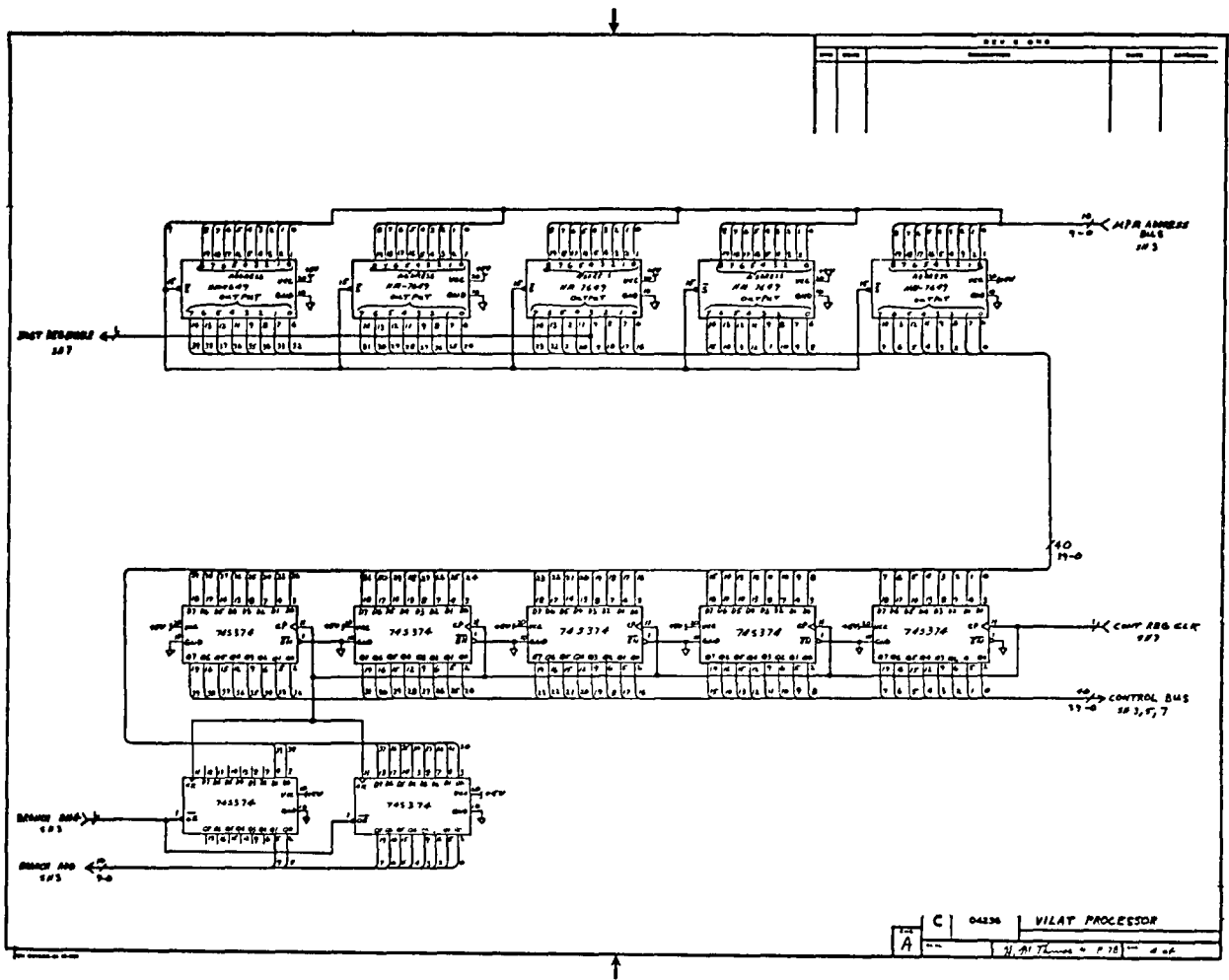


Figure 35 VILAT Processor Microprogrammer Memory Logic Diagram



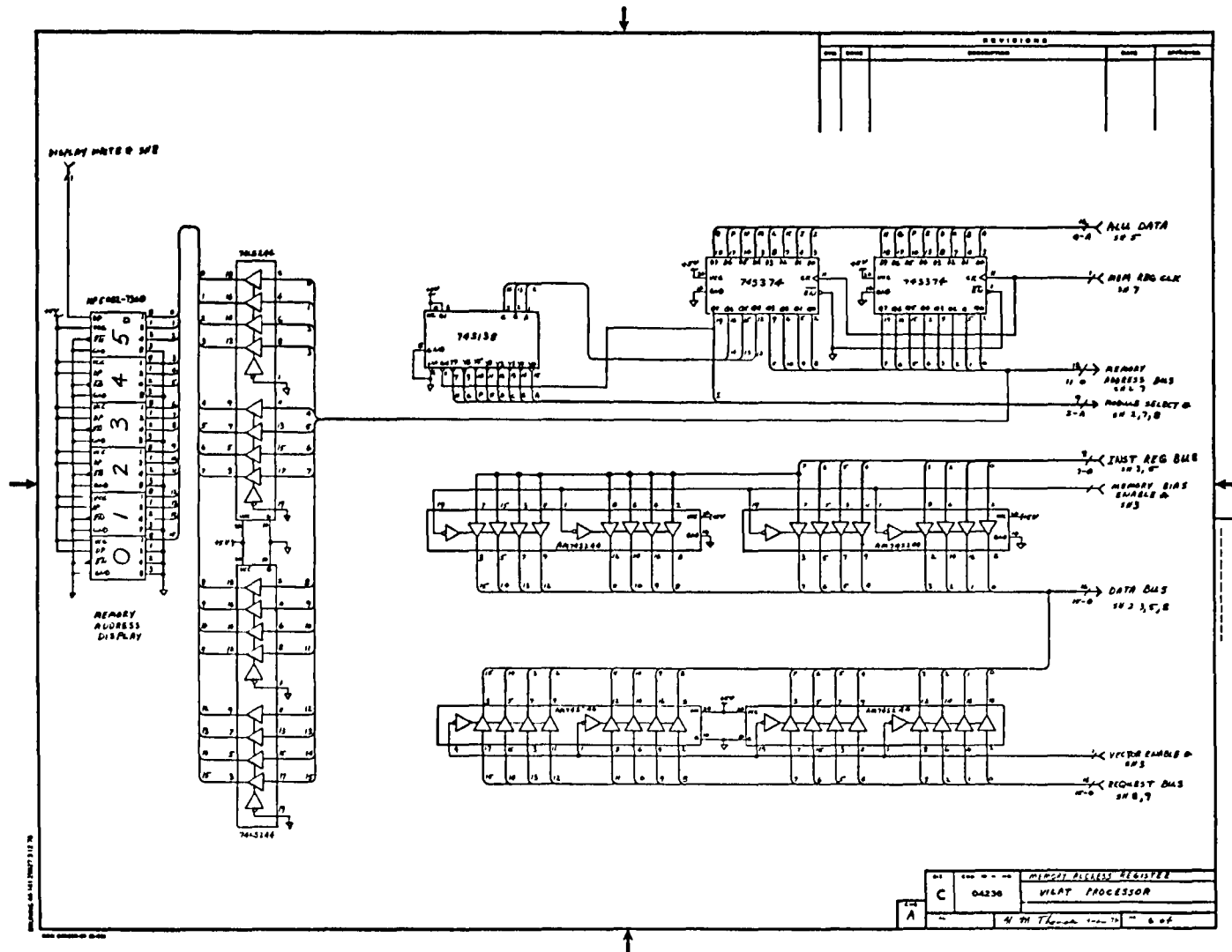


Figure 37 VILAT Processor Memory Address Register Logic Diagram

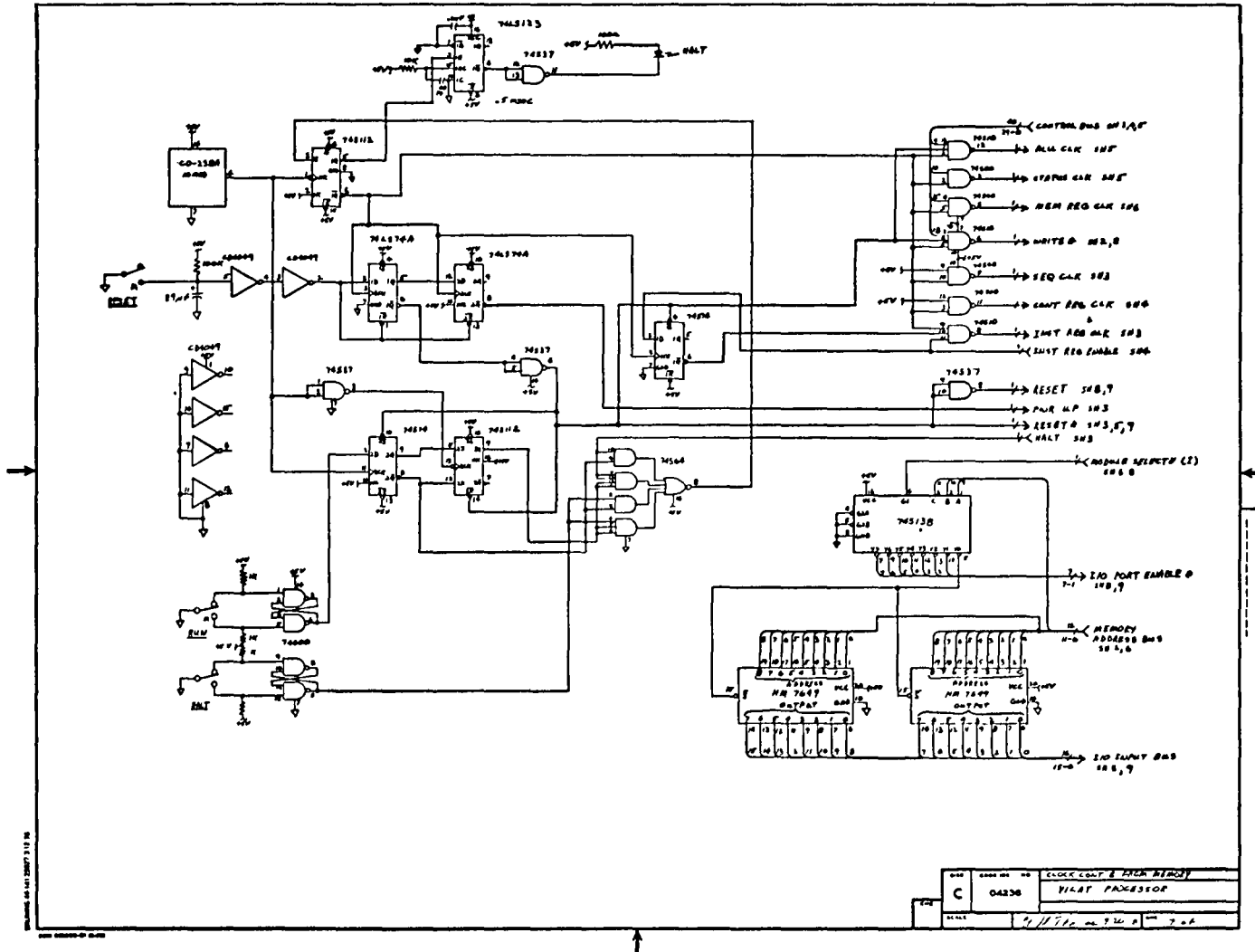


Figure 38 VILAT Processor Clock Control and PROM Memory Logic Diagram .





The Arithmetic and Logic Unit (ALU) (Fig. 32 and 36) provides the processor's computational capability. The heart of the ALU is the AM2901A microprocessor slice. The AM2901A contains an arithmetic unit, the eight general-purpose registers, and shifting logic. It receives control functions from the central control unit (CCU).

The clock control and CCU (Fig. 32, 34, and 38) provide control of all processor elements. The CCU sequences through the microprogram memory (Fig. 34 and 35), which contains the control words required to execute the processor instruction set. The CCU contains an instruction register, which holds the instruction word while the set of microprogram memory control words are sequentially executed to satisfy the instruction-word requirements. The instruction word is decoded by a series of mapping PROMs to determine the microprogram memory starting address for the required sequence of control words. The AM2911 microprogram sequencer is used for microprogram memory address control. The AM2911 contains an incrementer and multiplexer. The microprogram memory address may be the next sequential address, the map address, or a branch address from the control word being executed. The clock control generates the clocks required by the processor, under control of the control word being executed. The clock control also has manual reset, run, and halt capabilities.

Processor instructions are stored in a volatile random-access memory (Fig. 32 and 33). The memory address is held in the memory address register (Fig. 32 and 37). The address is calculated by the ALU and transferred to the memory address register. The memory address is also displayed on the processor control panel. A PROM memory (Fig. 38) provides nonvolatile storage of routines required to initialize the processor and load special-purpose programs.

The processor uses a request I/O structure. When an I/O device needs data from (or has data for) the processor, a request line is raised. There will be a request handler routine in the processor that will be executed when the processor is not busy with another task. Detection of the request will cause the processor to execute a routine to pass data to or accept data from the I/O device requesting access. This technique eliminates the time-consuming storing and restoring of general-purpose registers whenever a device requests access (which would be required with an interrupt system).

Four I/O functions will be provided: (1) an interface to the PDP 11/45 FILE simulation computer (Fig. 33); (2) an interface to the FILE breadboard (Fig. 33 and 40); (3) an RS-232C interface for standard computer peripherals (Fig. 32); (4) a control panel interface (Fig. 32 and 39).

The control panel is primarily used for checkout, troubleshooting, and software debugging. A 16-key keyboard is provided. Eight keys permit entry of the octal digits 0 through 7; the other eight are available for special functions. A data display is provided for monitoring keyboard entry and processor communication with the operator.

The RS-232C interface is a general-purpose I/O port for connection to standard computer peripherals or another computer for special tests. A paper-tape unit or cassette deck could also be connected for program entry without connection to a computer. A terminal could be connected for a more convenient operator interaction capability.

The FILE breadboard interface (Fig. 32 and 40) allows processor operation with live scenes from the breadboard. To automatically control breadboard operation, a control word is passed from the processor to the breadboard. Classified data from each cell are encoded in a 3-bit word. The interface then packs five of the cell words into one processor word and transfers it to the processor. An entire live scene can then be stored in the processor memory for later processing. A scene consists of 10,000 cells (100x100), which can then be packed into 2000 memory words.

The PDP 11/45 interface provides a high-speed parallel transfer between the processor and PDP 11/45. This will permit real-time interaction with FILE simulation at various stages in the program. As more capability is transferred to hardware, the processor will play a bigger role in the interaction. Initially, the processor will merely pass live scene data to the simulation computer; whereas, in the final stages, the simulation computer will merely pass scene data to the processor, which controls the test.

## VI. NEW CONCEPTS FOR ADVANCED FILE-TYPE EXPERIMENTS

---

A number of techniques can be included in future FILE-type experiments with the same basic hardware described in Chapter V. The hardware has computational capabilities and is designed to accept additional devices such as special scene processors, alternative sensors, and various mass storage devices. With these capabilities in mind, we investigated techniques for incorporating landmark registration in the VILAT processor, and have simulated the techniques in the Martin Marietta Image Processing Facility (Fig. 41). The facility can be separated into four areas: an interactive display, peripheral storage, central processor, and a hardcopy output line printer. These functional areas are connected by a common data bus that permits interfacing between any two. The central processor consists of a PDP 11/45 with 128K RAM memory that houses the software package designed for VILAT.

The peripheral storage area consists of two floppy disks (256K bytes each), two disk packs (2.5M bytes each), and four tape drives (two seven-track and two nine-track). The total memory capacity of the configuration is 5.5M bytes, not counting the tape drives, which are slow to access but extend the memory capacity indefinitely. The interactive display is composed of a RAMTEK random-access video display unit with 240 lines by 320 elements. Interaction is made possible through use of a keyboard and joystick that interfaces through several software packages to control the display.

The ultimate goal of adding registration techniques to the processor is to develop the capabilities of autonomous navigation, sensor data registration, and commanded sensor pointing aboard an advanced FILE-type experiment. Two registration techniques were investigated under VILAT and a related IR&D task, and are described in the following sections.

### A. LANDMARK REGISTRATION SIMULATION

The concept of using landmarks to register images is common in image processing. Landmarks (also known as Ground Control Points (GCP), Registration Control Points (RCP), or anchor points) are small images with known geophysical coordinates. The known landmark is found in a larger scene, and thus the larger scene (at least the local area in the scene) is registered. The technique involves finding the best fit of a "chip" in a "window." A chip is a small image (size varies from 8x8 pixels to 32x32 pixels) of known latitude and longitude. The window is a large area to be

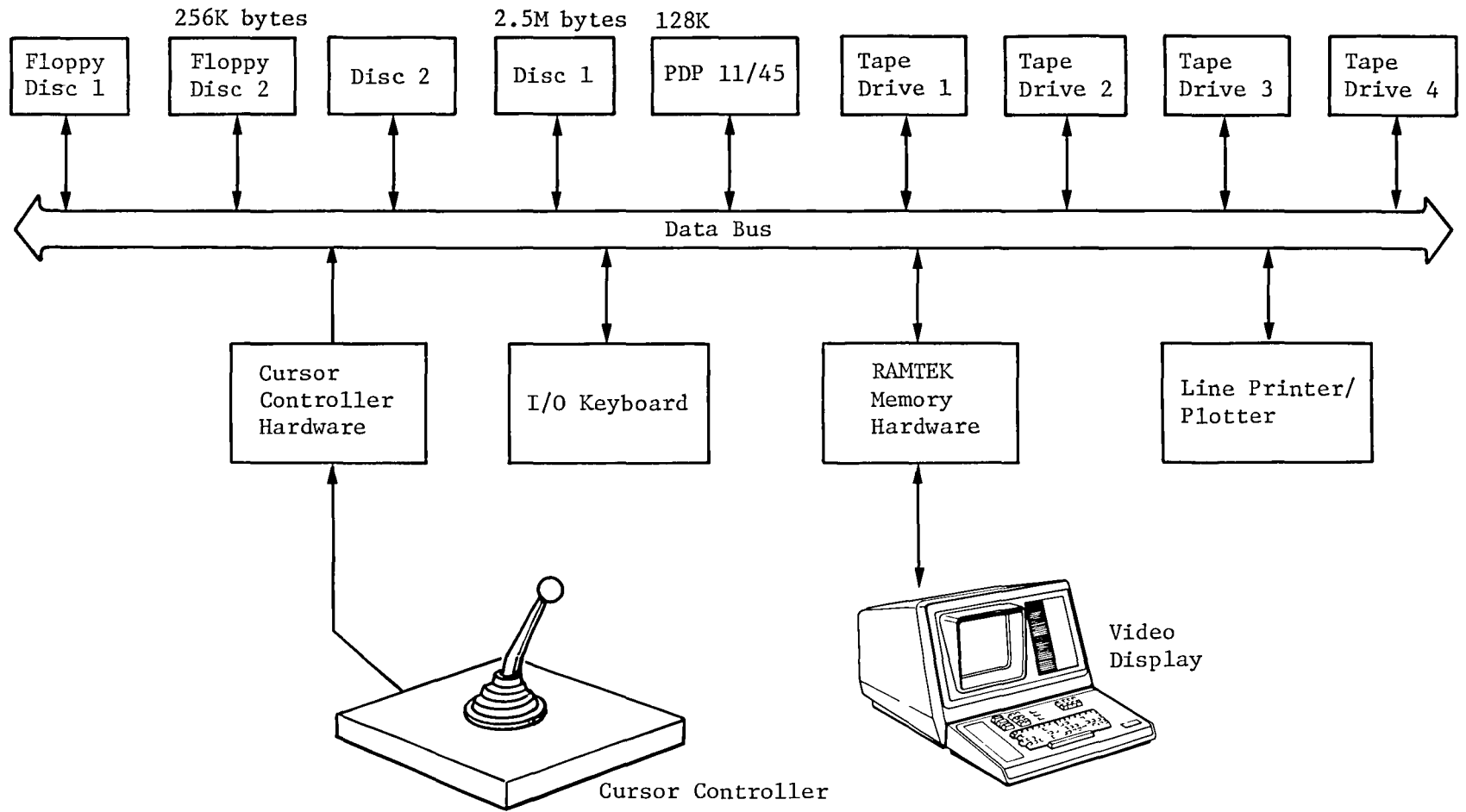


Figure 41 Image Processing Facility

searched--its size appropriate to the match position uncertainty. Figure 42 demonstrates the relationship of a chip-window pair. By finding the location of the chip in the window, the whole image can be registered.

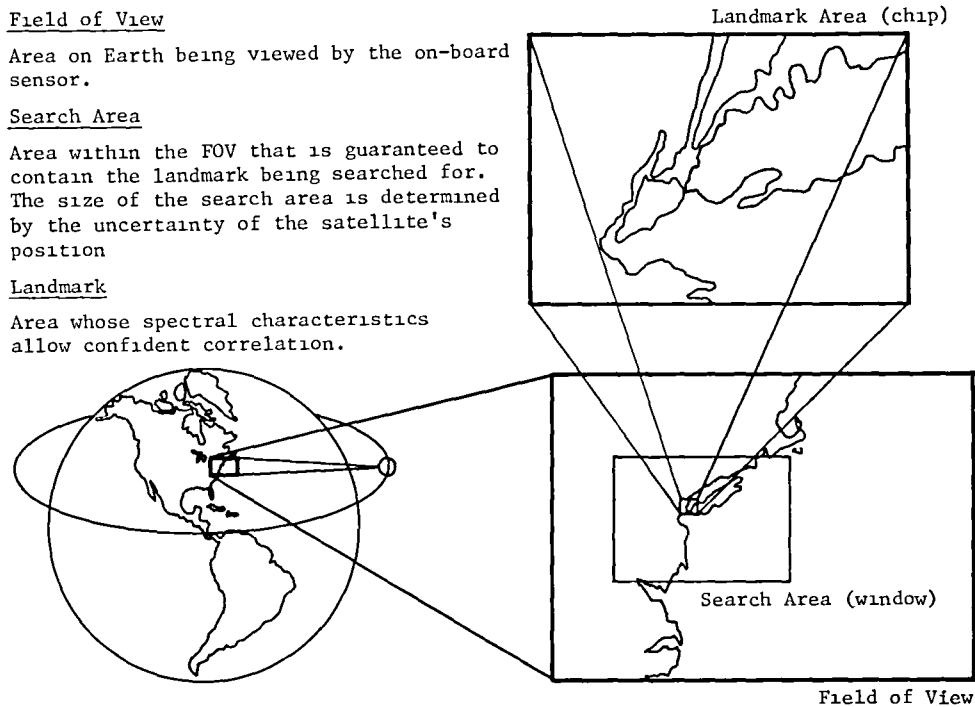


Figure 42 Relationship between Landmark and Search Area

Registration consists of comparing the stored landmark chip to all possible locations in the search area by a correlation algorithm. In our simulation, comparison begins in the upper left-hand corner of the search area (SA) and continues from left to right and top to bottom until every possible placement has been correlated. (Fig. 43). With this procedure, a three-dimensional correlation surface is formed, and the peak of the surface (or valley) corresponds to the location of the best fit.

When two similar LANDSAT video tapes are used, the landmark detection simulation developed under VILAT and an internal research task can register a user-selected chip (an array of pixels representing a significant landmark) taken from one video tape with respect to a search area taken from the second video tape (the same scene at a different time) to within 1/10 pixel accuracy. The two-tape process is intended to simulate an autonomous system in which a sensor/processor unit would correlate a prestored landmark area with image

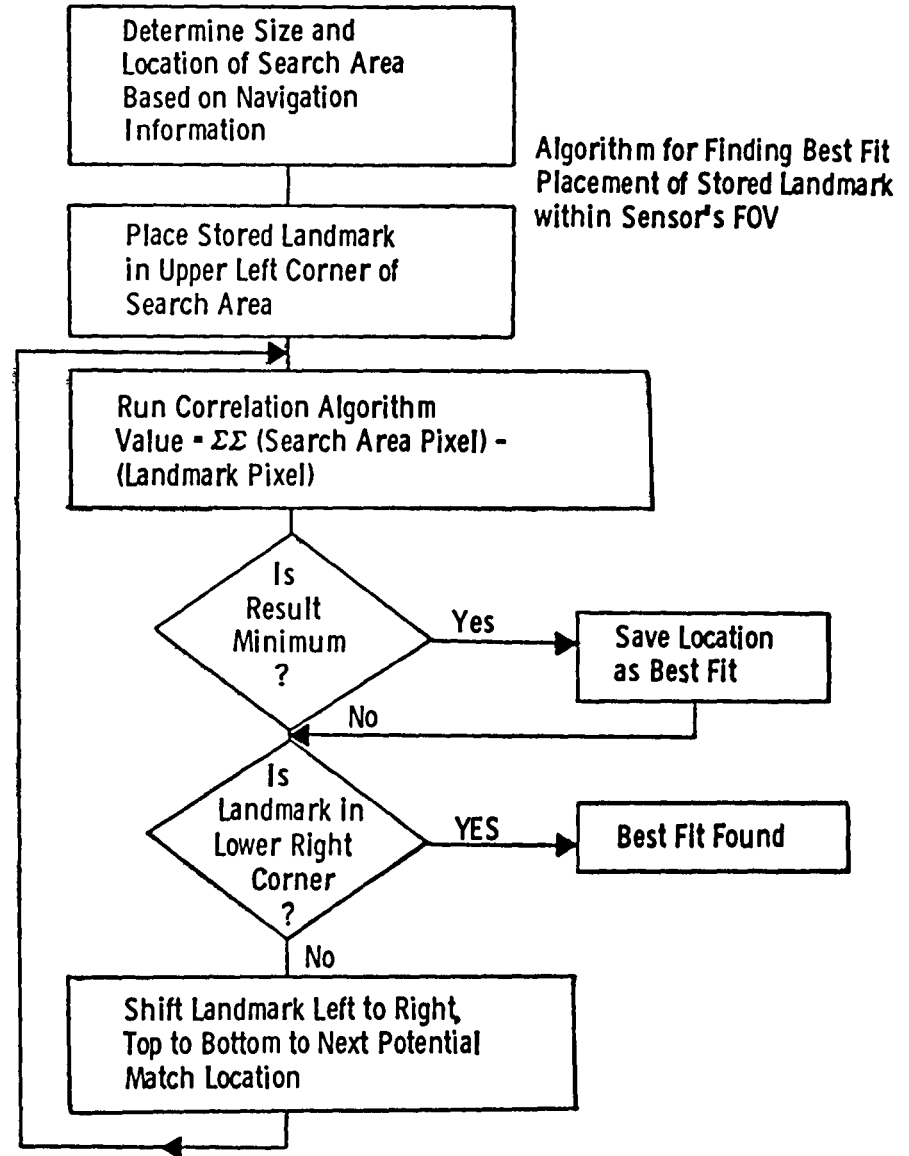
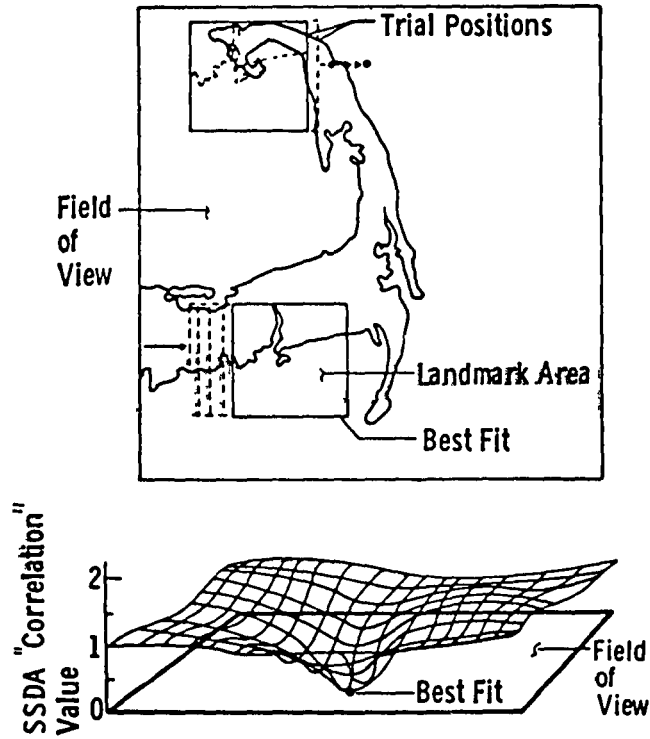


Figure 43 Registration of Area Landmark

data received from the sensor to combine latitude, longitude, and time information with video data. Figure 45 shows the organization of the software. The heart of the program is in the correlation algorithm and a resampling technique. These components allow registration to subpixel accuracy.

In Figure 44 the sections of the program required in a flight system have been outlined, the other sections are only pertinent to the simulation and would not be present in the flight software. The outlined portion of the software requires approximately 3000 16-bit words of memory plus additional memory for a landmark file. This size is compatible with state-of-the-art on-board processors.

Two correlation algorithms have been implemented (Fig. 45) and their results evaluated. On first evaluation, the classical correlator algorithm involving square roots and products of the pixel values was found to be inferior to the sequential similarity detection algorithm (SSDA), which involves only the sums of absolute differences between chip and window pixel values. Not only is the classical correlator slower (because of the added multiplication), making it less applicable to real-time operation, but the algorithm converges more slowly than the SSDA, suggesting less accuracy as well.

The SSDA has the added advantage that a decreasing threshold can be implemented to reduce the processing time. Because the algorithm converges toward zero as the similarity increases, a threshold can be established so that if, during calculation of the correlation coefficient, the SSDA sum exceeds some threshold value, computations are halted and the current position is known not to be the best fit. On the other hand, if the threshold value is not exceeded, the present landmark placement becomes the best fit and the new SSDA sum becomes the threshold for future calculations. This type of procedure cannot be implemented with the classical correlator (which employs an algorithm that converges toward a maximum value as similarity increases) because all the calculations must be performed before any correlation information can be obtained. Though the SSDA does not employ the classical correlation algorithm to perform correlation, it does find the coordinates of best fit and is therefore frequently called a correlation algorithm in the literature.

Registration to subpixel accuracy can be implemented in one of two ways: (1) the correlation surface can be interpolated; or (2) the image can be resampled at 1/10th of the interpixel distance and correlation around the best match location repeated. The second method was chosen because studies show that it achieves greater accuracy. Resampling involves interpolating between the discrete points on the intensity curve (Fig. 46) to form a new image surface that has been "shifted." Of the several resampling techniques implemented (Fig. 47), no one algorithm is clearly superior to all others.

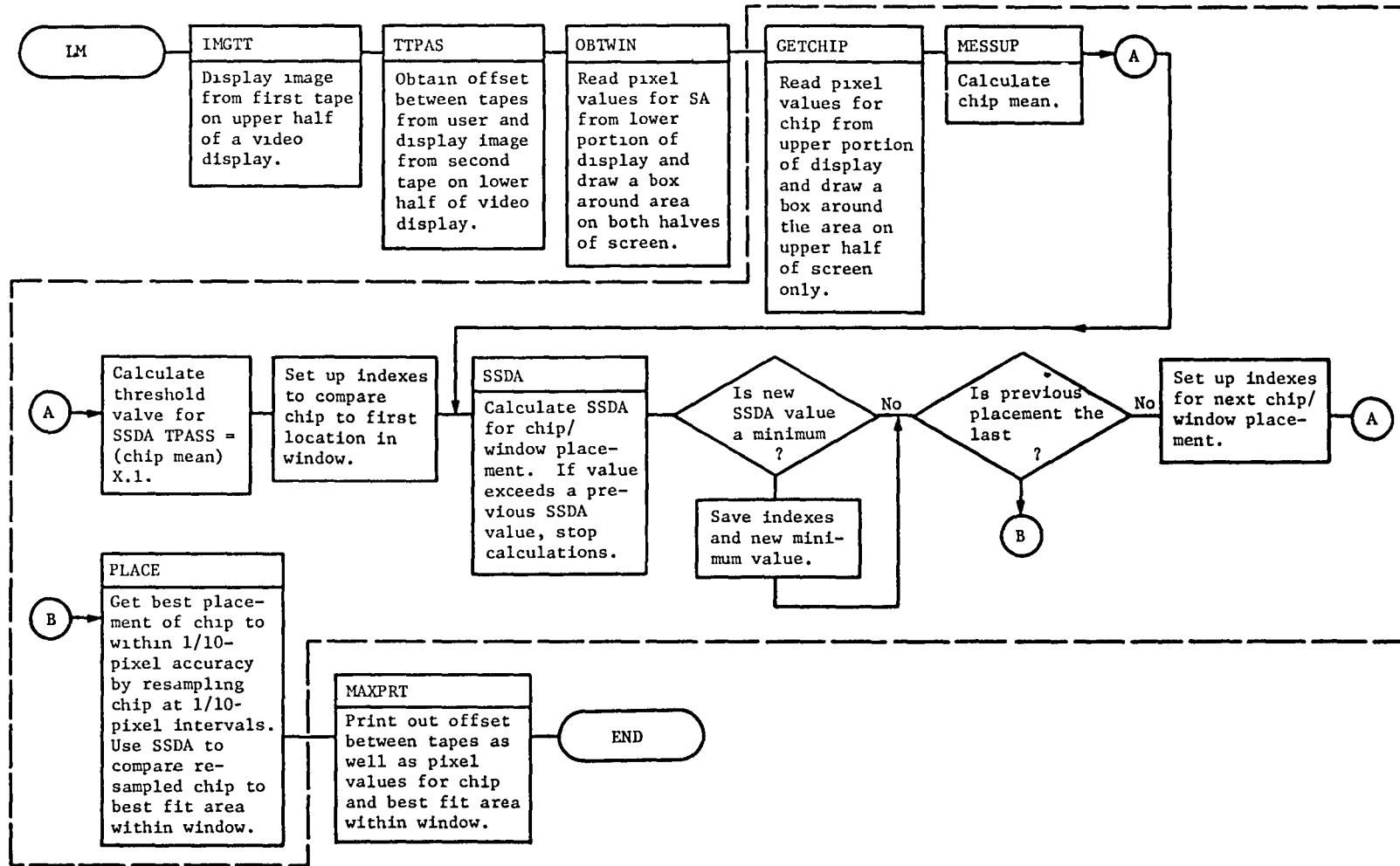


Figure 44 Organization of Landmark Identification Program

1) Sequential Search Detection Algorithm (SSDA)

$$SSDA = \sum_{i=1}^n \sum_{j=1}^n \left[ (\text{Chip}(i,j) - \text{Chip mean}) - (\text{Window}(i,j) - \text{Window Mean}) \right]$$

2) Classical Correlation =

$$\sum_{i=1}^n \sum_{j=1}^n \left[ (\text{Chip}(i,j) - \text{Chip Mean})(\text{Window}(i,j) - \text{Window Mean}) \right]$$

$$\left[ \sum_{i=1}^n \sum_{j=1}^n (\text{Chip}(i,j) - \text{Chip Mean})^2 \sum_{i=1}^n \sum_{j=1}^n (\text{Window}(i,j) - \text{Window Mean})^2 \right]^{\frac{1}{2}}$$

where:

Chip (i,j) is the (i,j)<sup>th</sup> pixel value in the n x n array of pixels representing the landmark.

Window (i,j) is the (i,j)<sup>th</sup> pixel in the n x n segment of the m x m array of pixels representing the overlapping area of the search area and the chip position.

$$\text{Chip Mean} = \sum_{i=1}^n \sum_{j=1}^n \text{Chip}(i,j) / n^2$$

$$\text{Window Mean} = \sum_{i=1}^n \sum_{j=1}^n \text{Window}(i,j) / n^2$$

Figure 45 Correlation Algorithms

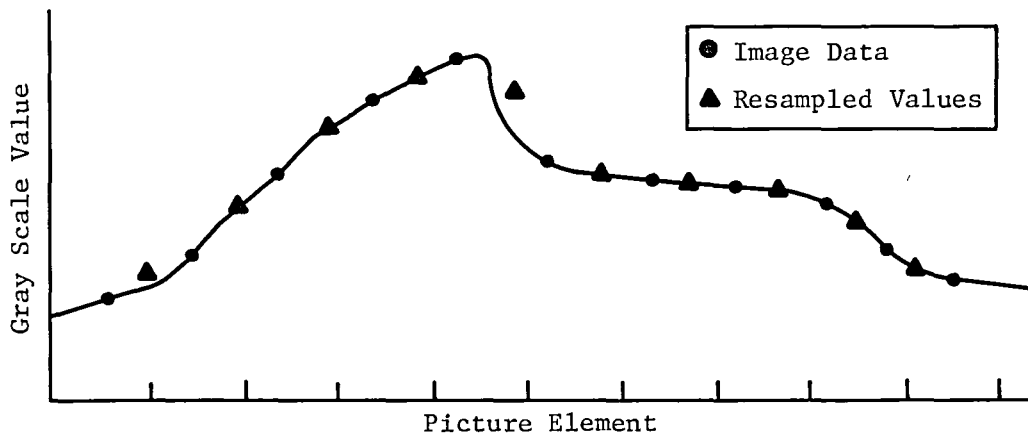
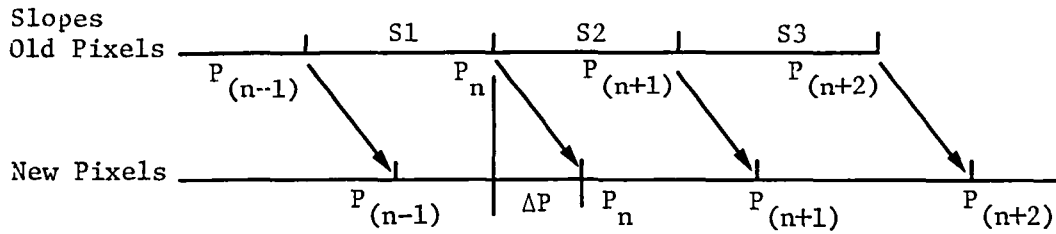


Figure 46 Two-Dimensional Resampling of Intensity Curve

The cubic convolution (CC) approach involves a cubic equation interpolation between pixels. When a smooth curve (corresponding to gentle features such as rolling hills) is being interpolated, the CC approximates the transition very well. However, when discrete features such as road crossings are used, the CC tends to smooth over the sharp transition between pixels. Because the SSDA correlation algorithm is best suited to sharp transitions and the CC tends to be a slower method of resampling, the CC will be ignored for the present.

The bilinear algorithm is satisfactory when coarse data are used. However, this and the nearest neighbor algorithm tend to ignore the peak of the curve. The bilinear approach follows the intensity curve when the two surrounding slopes have the same sign as the slope of the segment being interpolated. When the two surrounding slopes have opposite signs, the algorithm fails to compute the correct value. An algorithm we labeled the bilinear exaggerator (Fig. 44) was designed to correct this problem. During smooth transitions in which the three slopes have the same sign, a bilinear interpolator is used. When a sharp transition is encountered in which the surrounding slopes have opposite value, the exaggerator (which averages previous and current slopes to obtain a new pixel value) is used to magnify the transition. Although the bilinear exaggerator is a faster algorithm and appears to be better suited to landmark recognition, the cubic convolution interpolator should be reevaluated because it is more widely accepted in scientific circles.



Bilinear  $P_{n_{new}} = P_{n_{old}} + S2 + \Delta P$

Nearest Neighbor  $P_{n_{new}} = P_{n_{old}}$  where  $P_{n_{old}}$  is the nearest whole pixel

Bilinear Exaggerator

	Slopes			New Pixel Value
	S1	S2	S3	
Case 1	+	NA	-	$P_{n_{new}} = P_{n_{old}} + \frac{(S1+S2)}{2} (\Delta P)$
Case 2	-	NA	+	"
Case 3	0	-	+	"
Case 4	0	+	-	"
Case 5	+	-	+ or 0	"
Case 6	-	+	- or 0	"
All others	NA	NA	NA	$P_{n_{new}} = P_{n_{old}} + (S2) (\Delta P)$

Cubic Convolution

$$P_{n_{new}} = K_1 P_{n-1_{old}} + K_2 P_{n_{old}} + K_3 P_{n+1_{old}} + K_4 P_{n+2_{old}}$$

where:

$$K_1 = C_1 - C_2 (1 + \Delta P) + C_3 (1 + \Delta P)^2 - C_4 (1 + \Delta P)^3$$

$$K_2 = C_5 - C_6 (\Delta P) + C_7 (\Delta P)^3$$

$$K_3 = C_5 - C_6 (1 - \Delta P)^2 + C_7 (1 - \Delta P)^3$$

$$K_4 = C_1 - C_2 (2 - \Delta P) + C_3 (2 - \Delta P)^2 - C_4 (2 - \Delta P)^3$$

For landmark detection program:

$$C_1 = 4 \quad C_2 = 3 \quad C_3 = 5 \quad C_4 = 1 \quad C_5 = 1$$

$$C_6 = 2 \quad C_7 = 1$$

Figure 47 Resampling Algorithms

Use of the SSDA correlation algorithm to achieve subpixel accuracies has been examined in the Image Processing Facility. The programs were written in FORTRAN, with no attempt at optimization with respect to size or speed of execution, with one exception--a moderate attempt was made to use fixed-point arithmetic whenever possible. The PDP 11/45 executes fixed-point arithmetic in 2 to 4 microseconds, whereas a floating-point add requires 7 microseconds, and a multiply requires 10 microseconds. The time required for registration varies with the size of the landmark and search area and is summarized in Tables 6 and 7.

The times shown in Tables 6 and 7 reflect the experimental mode of operation in which no decreasing threshold was used, so that analysis of the data could be more complete.

*Table 6 Whole-Pixel Search Timing Requirements*

<u>Window Size</u>	<u>Chip Size</u>	<u>Time Required (sec)</u>
40 x 40 pixels	30 x 30 pixels	8.8
40 x 40 pixels	26 x 26 pixels	12.3
40 x 40 pixels	22 x 22 pixels	14.3
40 x 40 pixels	18 x 18 pixels	14.3
40 x 40 pixels	14 x 14 pixels	12.3
40 x 40 pixels	10 x 10 pixels	8.8
32 x 32 pixels	16 x 16 pixels	3.6
76 x 76 pixels	16 x 16 pixels	69.5

*Table 7  
Subpixel Resample and Search  
Timing Requirements*

<u>Chip Size</u>	<u>Time Required (sec)</u>
30 x 30 pixels	19.0 to 27.0
26 x 26 pixels	17.0 to 18.0
22 x 22 pixels	10.0 to 13.0
18 x 18 pixels	8.5 to 10.0
14 x 14 pixels	4.5 to 6.0
10 x 10 pixels	2.5 to 3.0

Experiments show that a 6:1 improvement in execution time can be achieved by incorporating the decreasing threshold. The same studies also indicate that a 3:1 improvement in run time can be achieved if image resampling is linked to the SSDA and its decreasing threshold. Thus, pixels are only resampled until the threshold is surpassed. Improvements in execution time allow registration of an 18x18 landmark chip on a 40x40 window in 5 seconds.

Although autonomous landmark navigation is feasible, using state-of-the-art technology with 8-bit gray-scale data, the method has several shortcomings: time required for registration, effects of clouds on the registration process, and effects of seasonal variations. Experimental results showed that a nominal landmark search area could be registered in about 5 seconds. This time can increase to as much as 20 seconds if the uncertainty in position increases above expected values. Such registration times may be inadequate for the needs of a navigation system and will certainly not be adapted to a sensor pointing system. Cloud coverage in the search area causes a decrease in the accuracy obtainable and can result in a false lock of the correlator (Fig. 48). While a method of false-lock detection has been developed, the effects of missing a landmark sighting cause deterioration in the system's position accuracy. If several sightings are missed, the system may become divergent or uncontrollable. Just as clouds affect the system's registration accuracy, so do seasonal variations in the terrain. Such variations include snow coverage, spectra of vegetation, ice on lakes, etc.

The system's limitations led to a concept of using the preclassified data proved by FILE instead of gray-scale image data. Such data are 3 bits instead of 8, and pixels correspond to classification types such as clouds, bare earth, vegetation, and water. The 3-bit data will produce a significant decrease in registration time, and preliminary studies show that the process can be performed in approximately 10 milliseconds if the correlation algorithm is hard-wired. By incorporating classified data in the system, any picture element that represents snow, clouds, or ice can be ignored during calculations, significantly reducing the effects of these elements on correlation accuracy. The next section describes a simulation that was built around this idea under the VILAT program.

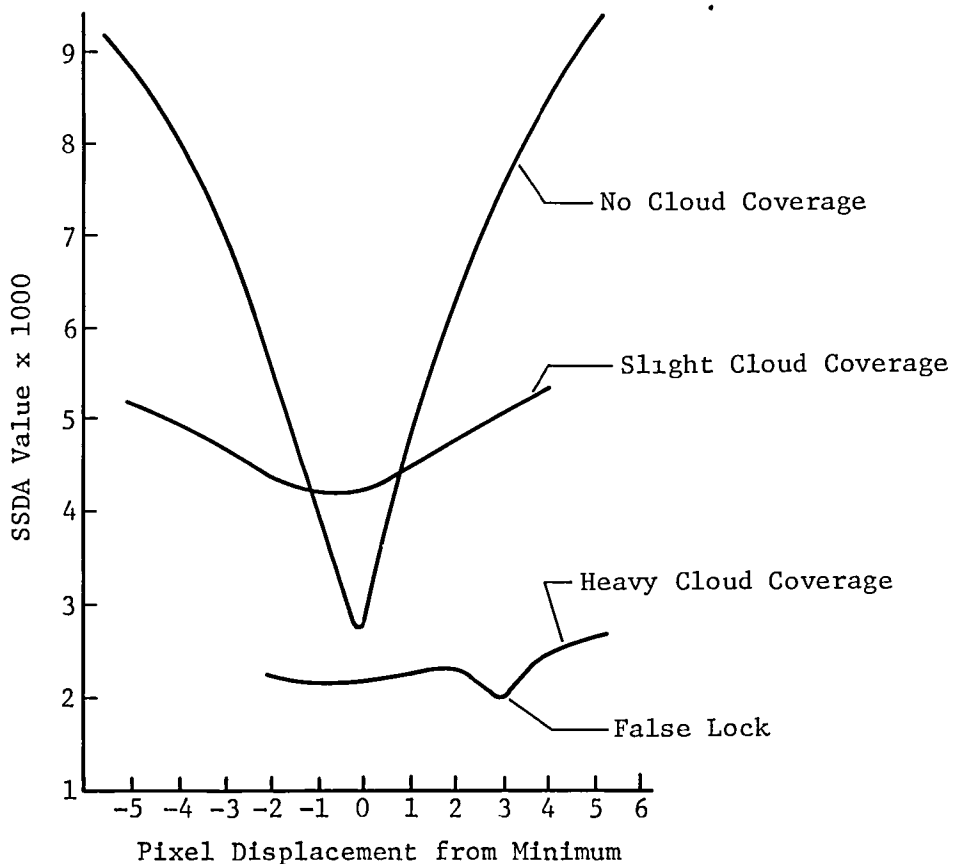


Figure 48 Effects of Cloud Coverage

B. ADVANCED FILE SIMULATION (MULTICOLOR REGISTRATION)

The present FILE experiment was simulated in the Image Processing Facility. Images in two parts of the spectrum were displayed, and classified using the multispectral ratio approach. In the basic simulation areas from two LANDSAT tapes (different exposure times) of the same scene in the 0.6 and 0.8 micrometer spectral region were video displayed. A pixel-by-pixel ratio was then taken of the two areas, and a video representation of the results displayed. The number of picture elements in each region shown below was then printed along with the picture-element values of the two scenes.

<u>Multispectral Ratio</u>	<u>Classification</u>
0.0 - 0.9	Vegetation
0.9 - 1.5	Ground, Snow,
1.5 - 3.0	Clouds, Ice
>3.0	Water

The basic FILE simulation was then incorporated in the landmark registration program so that the scope of an advanced experiment could be increased.

The unique use of multispectral data in landmark registration diminishes the severity of problems encountered in the previously mentioned registration technique. First, the ratioing scheme enhances otherwise indistinguishable features, thus permitting selection of landmarks from a broader area. The enhancement also ensures that the correlation surface will converge more rapidly toward a best fit. Second, the effects of various noise sources on the correlation process can be significantly reduced because the ratio technique eliminates variations in the mean radiance value, and picture elements representing clouds, snow, or ice (major noise sources) can be ignored during the correlation procedure even though they may be used by the experiment. Third, 3-bit data can be registered more quickly than 8- or 16-bit data, which will make autonomous navigation a more feasible goal.

The simulator proceeds as described below and shown in Figures 49 through 53. Input data consist of two sets of LANDSAT tapes of the same scene taken at two different times. Each tape set contains image data from bands six and seven of the LANDSAT multispectral scanner. The first segment of the program allows the user to select the coordinates of a scene from the image tapes, exposed at time  $t_1$ , and displays images from the two spectral bands on the upper and lower parts of the monitor (Fig. 49). A search area is then selected from these data with the interactive cursor (Fig. 49).

When the user has determined size and location of the search area, the upper part of the screen is erased and the search areas for each spectral band, as well as a video representation of the multispectral ratio are displayed (Fig. 52). The lower part of the screen is then erased and the search area data (band 1, band 2, and multispectral ratio) from the second set of LANDSAT tapes (exposed at time  $t_2$ ) is displayed (Fig. 51). The user then selects the size and location of a suitable landmark using the cursor (Fig. 51), and a box is drawn around the landmark area within the search area corresponding to time  $t_2$  (Fig. 52). In an onboard system, selection of the search area would be performed through algorithms that transform the position and attitude of the satellite into size and location of the search area. The correlation algorithm described in the previous section is then run using the landmark from the multispectral data at time  $t_2$  and the search area from the multispectral data at time  $t_1$ . A box is then drawn around the area of best fit in the search area (Fig. 53). All image data used in the simulation, as well as the correlation surface, are available to the user through printouts on the line printer.

Quantitative results of the advanced VILAT simulation have not been obtained because of the delay in delivery of LANDSAT data. However, preliminary results, in which the multispectral ratio was simulated, show that the multispectral ratio will bring unique benefits to the registration process.

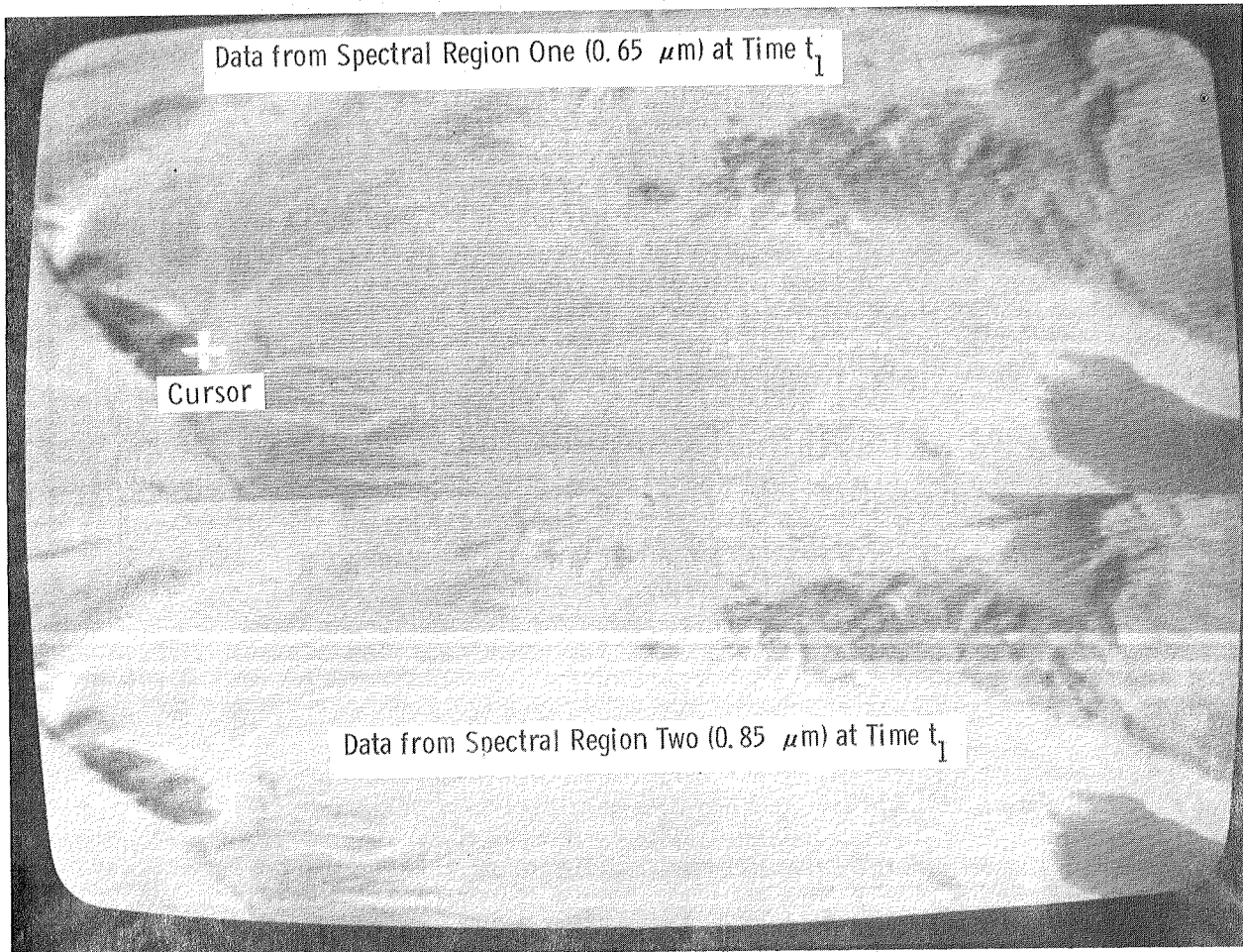


*Figure 49 Selection of Search Area*

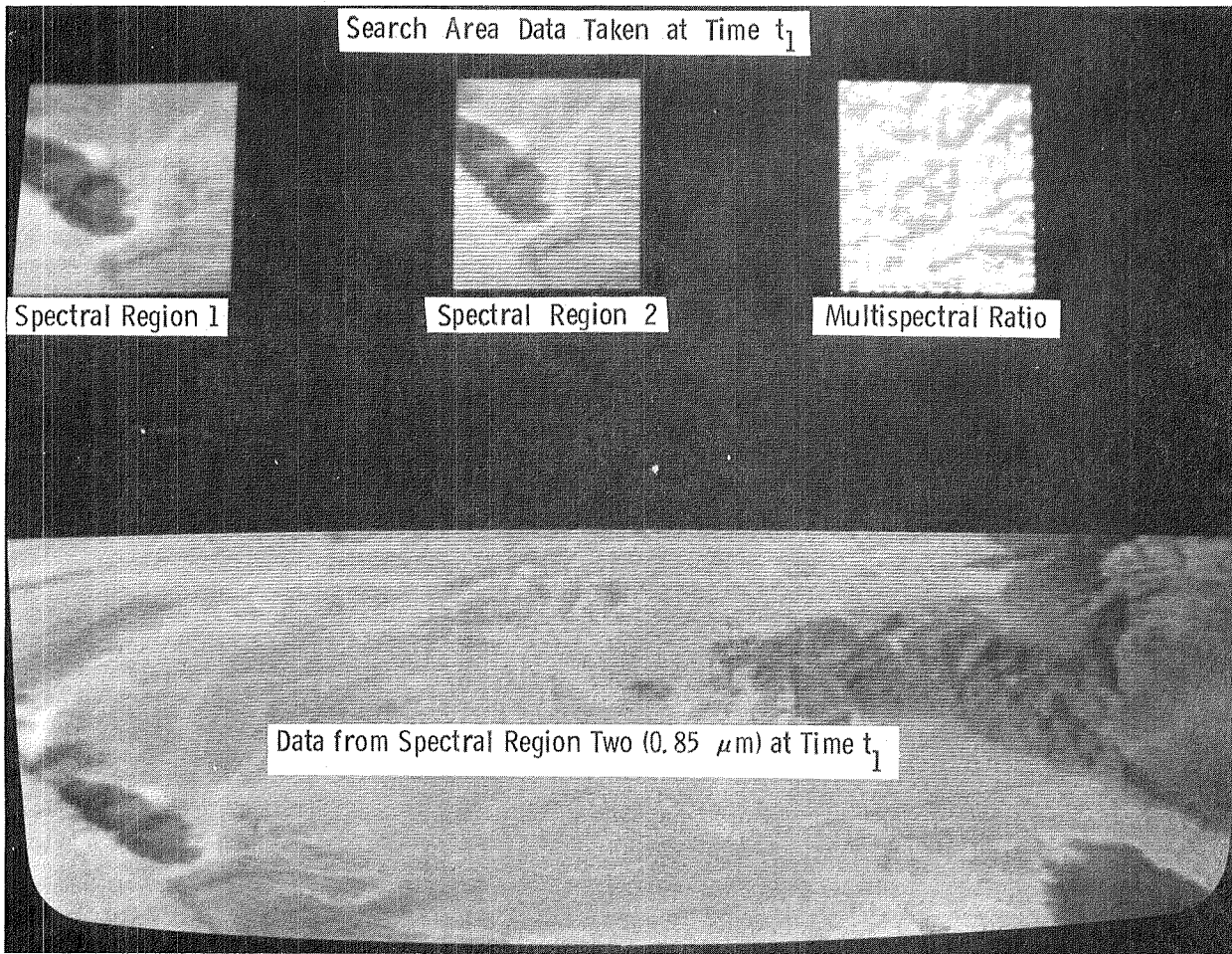


*Figure 50 Display of Search Area*

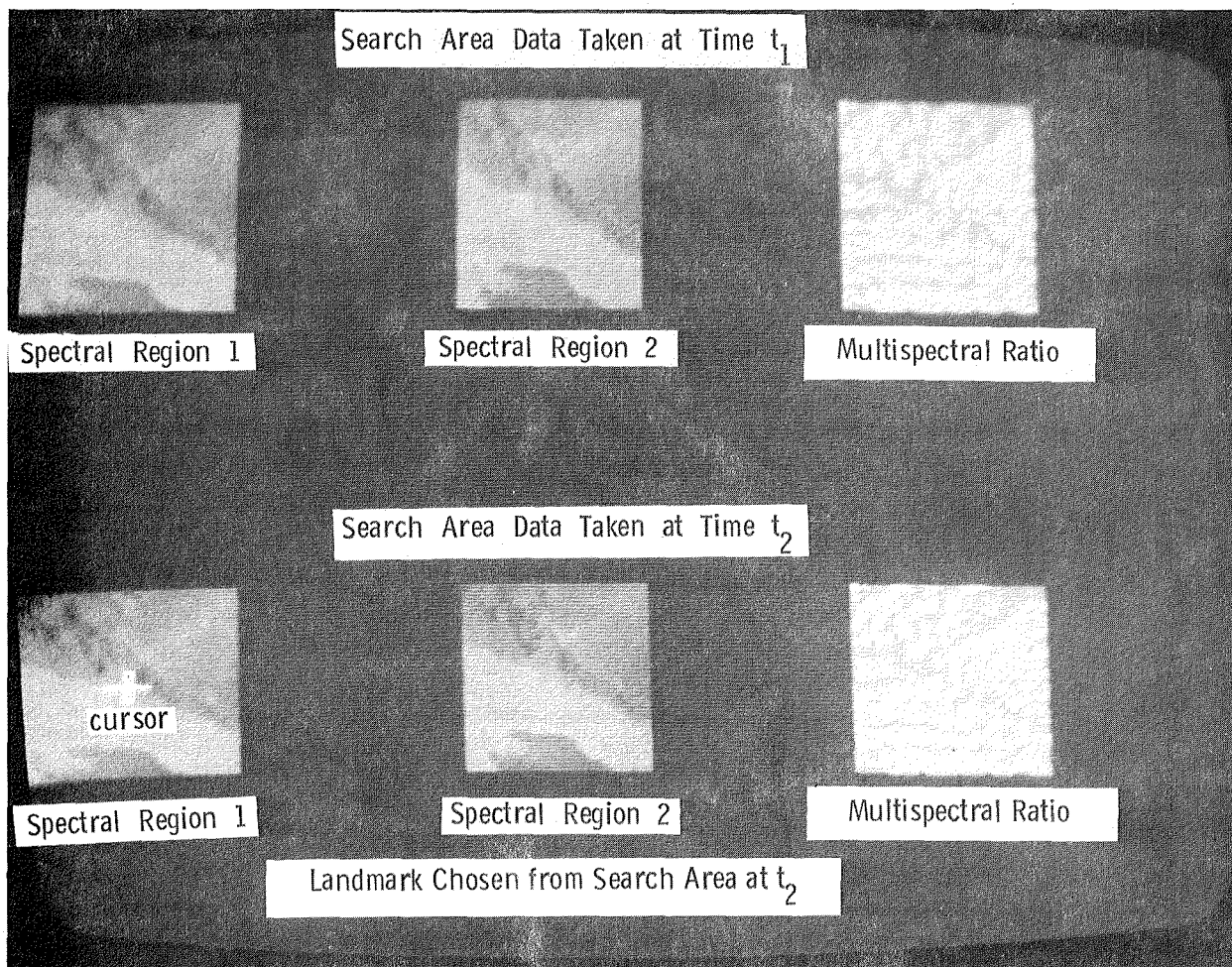
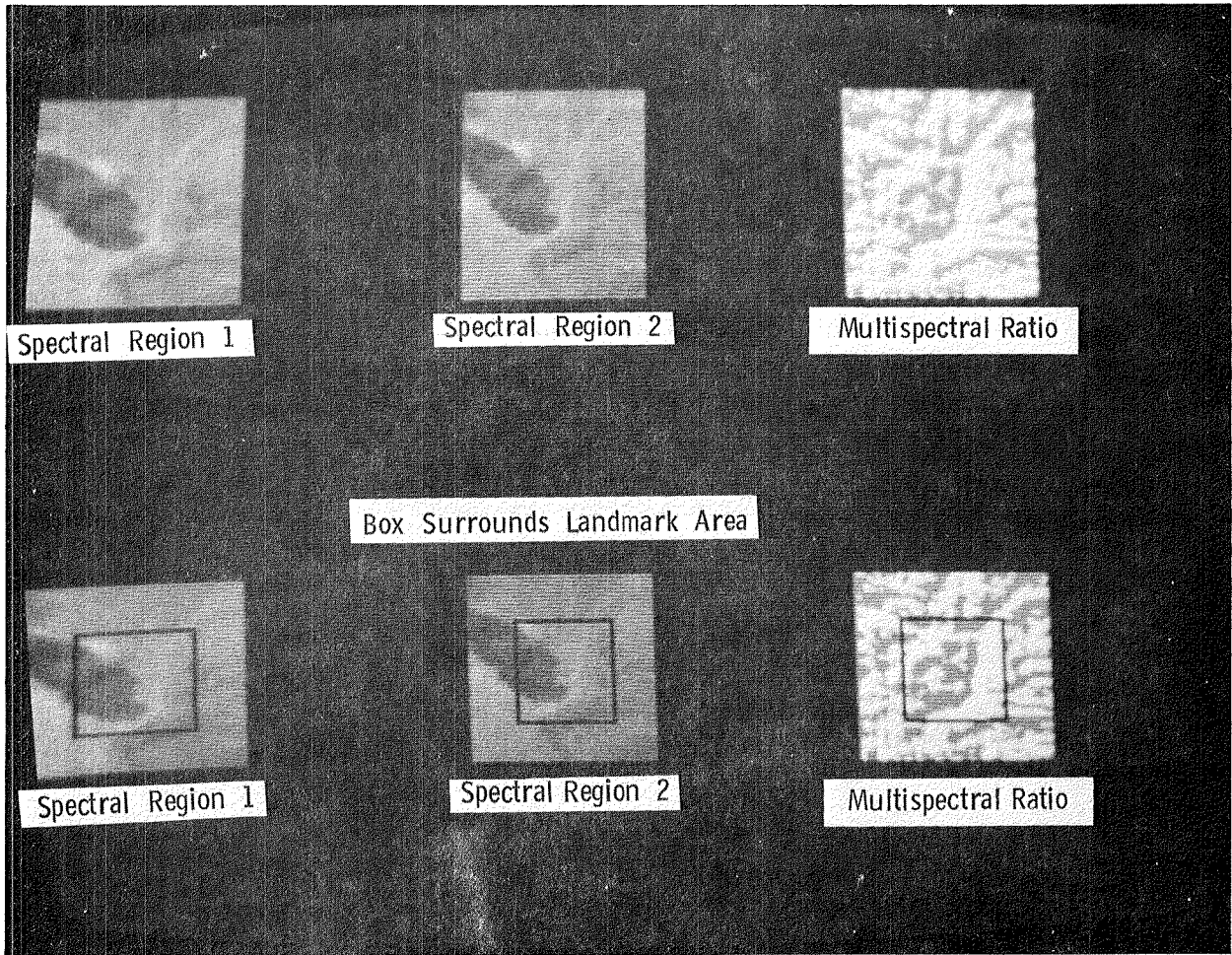
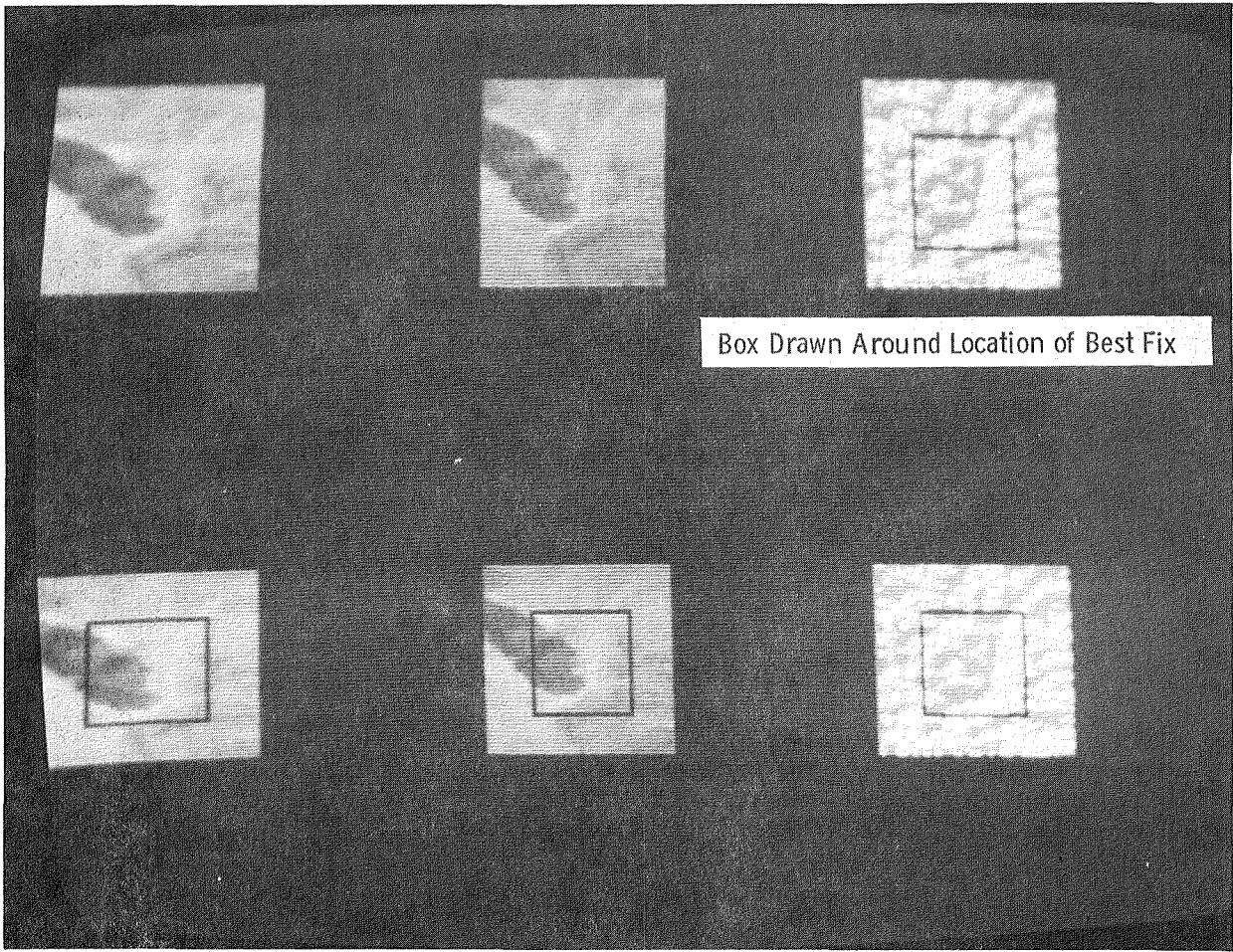


Figure 51 Selection of Landmark Area



*Figure 52 Display of Landmark Area*



*Figure 53 Display Correlation Results*

## VII. CONCLUSIONS AND RECOMMENDATIONS

---

Remote sensing has traditionally been unselective with respect to information content. This has greatly increased data archival costs, which are already becoming prohibitive, and has resulted in excessive delays between acquisition of the data and its eventual dissemination to users.

Furthermore, technological development of remote sensing systems has in many instances outstripped the corresponding development of interpretation methodologies and techniques that are essential for conversion of remotely sensed data into usable information, resulting in a voluminous backlog of raw data. New technologies are therefore required to limit the volume of raw data collected from satellites, through onboard preprocessing and data identification.

The activities described in this report have shown that adaptive "smart" sensors of this type are feasible and that they can be implemented using simple algorithms and a minimum of hardware. The techniques described herein should be incorporated in future FILE systems to demonstrate their feasibility in an orbital environment.

FILE I, the first such system, is nearing completion and is scheduled to fly in 1980. It will demonstrate autonomous data selection and classification of surface features on the basis of their spectral signatures through a very simple algorithm. Each of the succeeding FILE flights should test more of the techniques and capabilities, including autonomous pointing, tracking, correlation, and landmark navigation, in a realistic environment.

Specific recommendations with respect to the next step in the development of adaptive sensor systems are as follows.

- 1) Breadboard and perform laboratory testing of a cloud detection system;
- 2) Perform computer simulation studies to evaluate candidate concepts for developing a versatile pointing and tracking system;
- 3) Establish the rationale for a landmark acquisition technique;
- 4) Establish a plan oriented toward arriving at the fabrication and flight testing of a VILAT instrument with capability for acquisition, classification, pointing, tracking, and landmark navigation. This plan should contain cost projections, flight-test requirements, a development time-line, identification of technology risks, and specific recommendations for the next phase of development. Table 8 indicates the sequence of experiments that would evolve from the VILAT activity.

Table 8 Sample Outline of the VILAT Development Plan

<u>Shuttle Flight</u>	<u>Experiment Capabilities</u>
1980	FILE I - OSTA-1 Payload (Current Experiment on STS-2 or -3) <ul style="list-style-type: none"> <li>- Classification capability</li> <li>- Autonomous real-time operation</li> <li>- On-board decision logic</li> </ul>
1980-81	FILE II (FILE I Modified for Later STS Flight) <ul style="list-style-type: none"> <li>- Classification capability</li> <li>- Cloud, snow, and ice discrimination</li> <li>- Autonomous real-time operation</li> <li>- Enhanced on-board decision logic</li> <li>- Shuttle crew interaction capability for preselected target data acquisition</li> <li>- Ground truth site data acquisition</li> </ul>
1982	FILE III (FILE II Modified) <ul style="list-style-type: none"> <li>- Enhanced classification capability</li> <li>- Computational capability</li> <li>- Surface interface detection</li> <li>- Pointing and tracking capability</li> <li>- Shuttle crew interaction capability</li> </ul>
1983	FILE IV (FILE III Modified) <ul style="list-style-type: none"> <li>- Enhanced classification capability</li> <li>- Computational capability</li> <li>- Surface interface detection</li> <li>- Pointing and tracking capability</li> <li>- Area correlation capability</li> <li>- Registration and landmark navigation capability</li> <li>- TM uplink for target data</li> </ul>

VII. REFERENCES

---

1. Schappell, R. T., Tietz, J. C., Hulstrom, R. L., Cunningham, R. A., and Reel, G. M.: *Preliminary Experiment Definition for Video Landmark Acquisition and Tracking*, NAS CR-145122, (Contract NAS1-14489) Martin Marietta Aerospace, Denver, Colorado, December 1976.
2. Schappell, R. T., and Tietz, J. C: "Landmark Identification and Tracking Experiments," presented as paper 78-1702 at AIAA/NASA Conference on "Smart" Sensors, NASA Langley Research Center, Hampton, Virginia, November 14, 1978.

**End of Document**